Astroparticle Physics 2919/20

Lectures:

http://particle.astro.ru.nl/goto.html?astropart1920

lecture 10
Acceleration, Astrophysical accelerators and beam dumps
Gaisser chapter 14

14.3 Gamma ray bursts

Gamma ray bursts (GRBs) were discovered serendipitously in the late 1960s by the Vela satellites, originally designed to search for very fast and intense bursts of gamma rays produced by nuclear weapon tests in space [474]. GRBs are the most energetic transient events in the Universe, with an emitted energy up to 10^{53} erg. They are isotropically distributed, and hence extragalactic, as first observed by the Burst and Transient Experiment (BATSE) on the Compton Gamma ray Observatory (CGRO) [475]. GRBs show a highly variable temporal profile with $\delta T/T \sim 10^{-2}$, which still challenges present models. For a detailed review see e.g. [476].
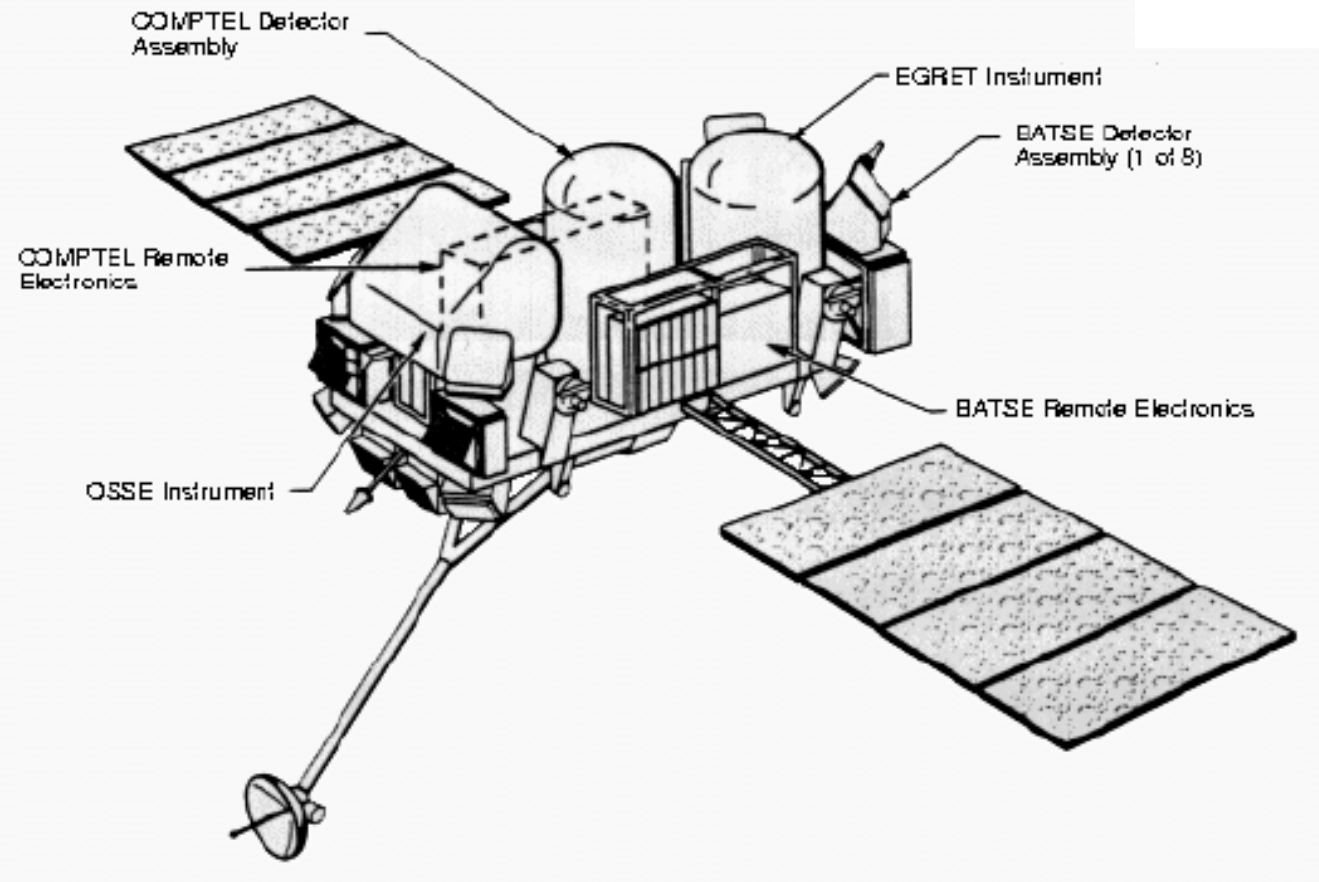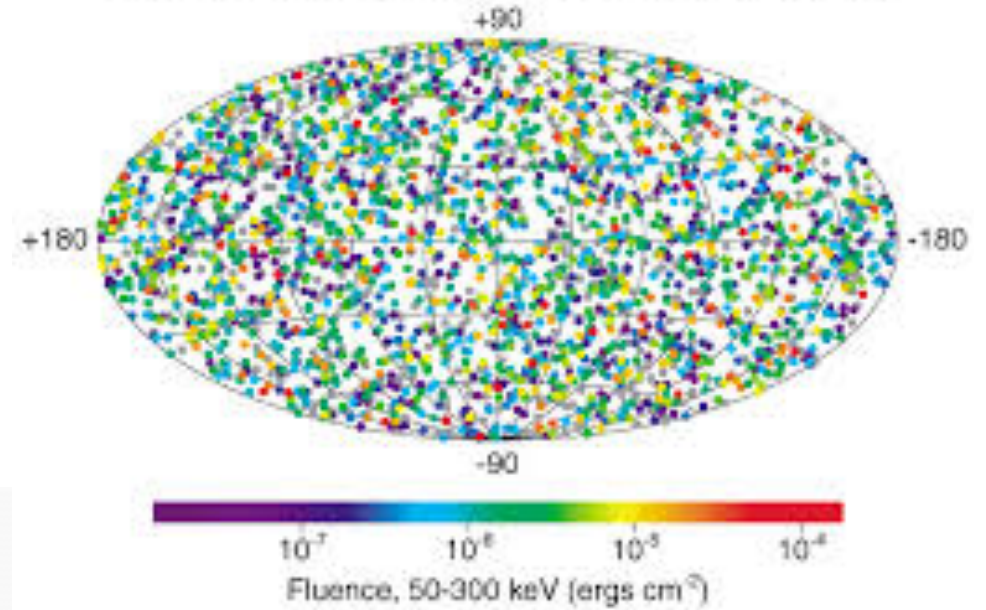
Two wide categories of prompt emission are traditionally identified: long bursts ($t > 2\,\mathrm{s}$) and short ones ($t < 2\,\mathrm{s}$). A physical basis for the distinction is emerging connected to the progenitor type: collapsar or non-collapsar [477]. Long bursts are most probably connected to the catastrophic deaths of a massive star collapsing into a black hole [478], while the short ones may correspond to the merger of compact object binaries [479, 480]. Both types of emission are followed by a longer-lived *afterglow* radiation. The first detection of afterglows from long GRBs was obtained by the Beppo-SAX satellite in 1997, eight hours after the main burst of GRB 970228. The X-ray transient was followed up by a multi-wavelength campaign that revealed a fading transient at the position of the GRB [481]. An afterglow is consistent with the picture of the slowing down of a relativistic flow as it expands into the surrounding medium. Observations of afterglows can provide key information about the host galaxy, the distance and precise positioning of the GRBs.

Number of bursts vs Time (seconds)

2 seconds

Short-duration bursts ← | → Long-duration bursts
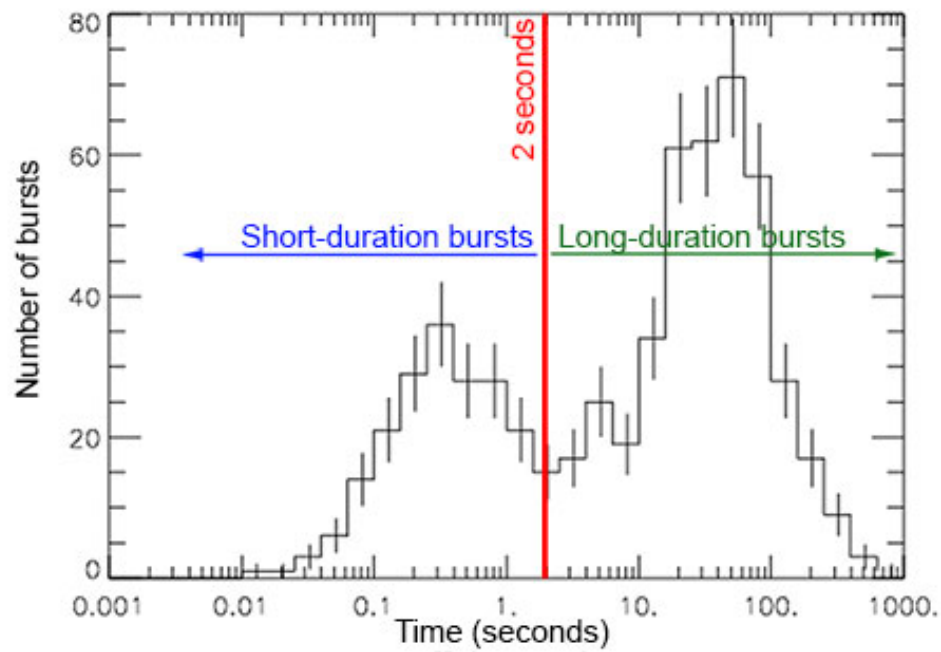
2704 BATSE Gamma-Ray Bursts

Fluence, 50-300 keV (ergs cm⁻²)

COMPTEL Detector Assembly

EGRET Instrument

BATSE Detector Assembly (1 of 8)

COMPTEL Remote Electronics

BATSE Remote Electronics

OSSE Instrument

14.3.1 Collapsars: long gamma ray bursts

Collapsars are powered by accretion of a massive disk formed around the black hole [482]. Relativistic jets are formed which punch through the outer layers of the progenitor and then into the surrounding medium as illustrated in Figure 14.8. This scenario has found observational support through the association of GRB afterglows with their progenitor core-collapses. The first direct evidence of the GRB/core-collapse connection was gained through the study of the relatively close by GRB 030329 ($z = 0.1685$) and its associated very energetic type Ic supernova (*hypernova*) SN2003dh [483]. The supernova light curve emerged from the GRB afterglow within ten days and was spatially coincident with the GRB. The broad lines in the supernova spectrum indicate an initial expansion velocity of more than $\approx 36,000$ km/s.

Three principle phases are identified in the *collapsar model*:

- Massive star core-collapse: a massive star ($M > 30 M_\odot$) with an iron core (1-2 $M_\odot$) undergoes a core-collapse. This results in formation of a black hole, either directly or via an accretion phase.
- Accretion disk formation: around the collapsed core a cylindrically symmetric accretion disk is formed with its symmetry axis parallel to the rotation axis. The disk accretes at a rate of about 0.5 $M_\odot$/s, amplifying entrained magnetic fields and injecting energy into the surrounding medium.
- Jet initiated fireball: matter is expelled preferentially along the rotational axes in form of a two-sided jet ($\theta_{jet} < 10°$), sometimes referred to as *fireballs*.

The existence of jets in GRBs is inferred from the study of the light curves of the afterglows and from polarization studies [484].
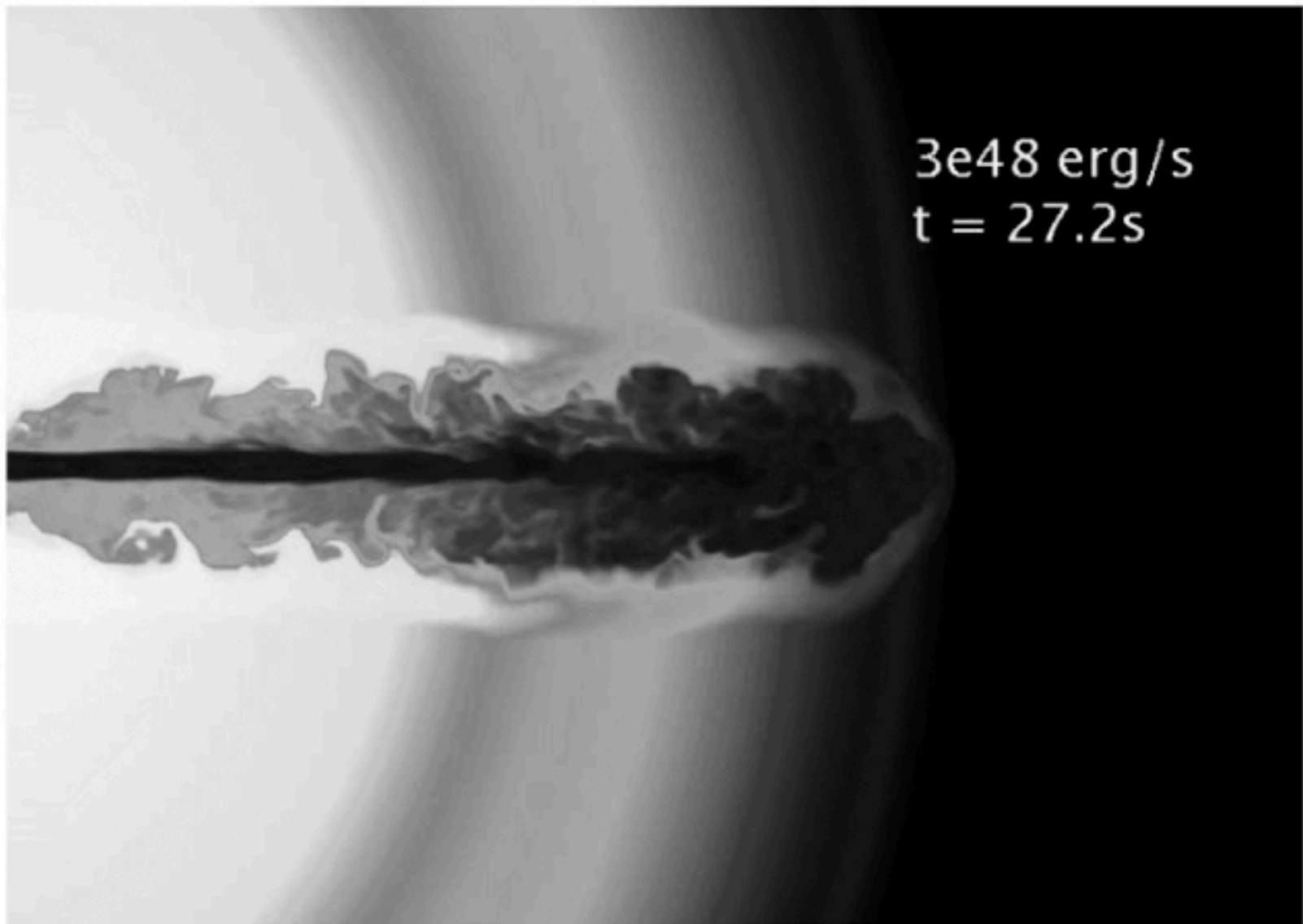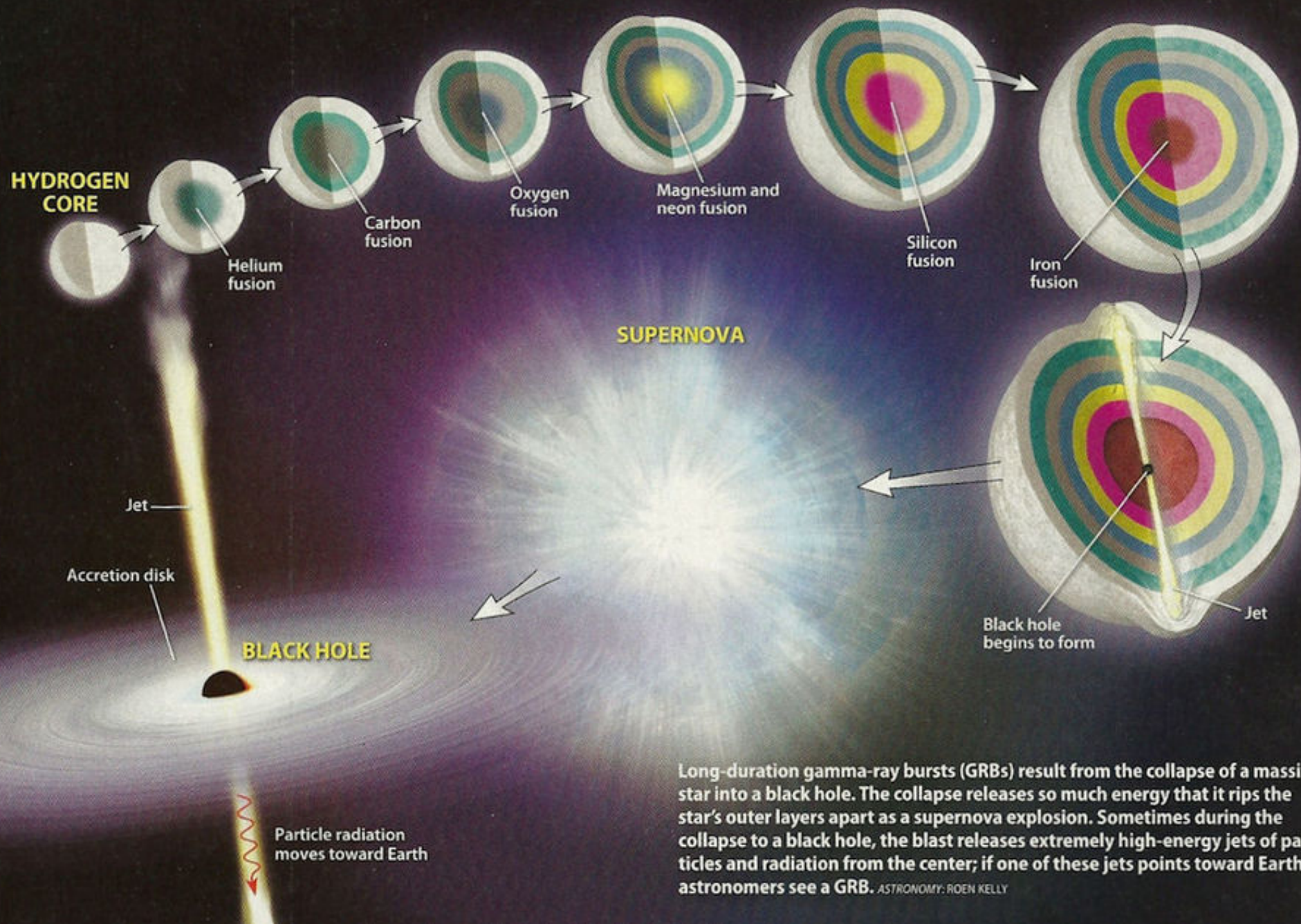
Figure 14.8 Three-dimensional modelling of a relativistic jet injected from the center of a 15 $M_\odot$ Wolf–Rayet star. Picture taken from [476].

From a supernova to a gamma-ray burst

HYDROGEN CORE

Helium fusion

Carbon fusion

Oxygen fusion

Magnesium and neon fusion

Silicon fusion

Iron fusion

SUPERNOVA

Black hole begins to form

Jet

Jet

Accretion disk

BLACK HOLE

Particle radiation moves toward Earth

Long-duration gamma-ray bursts (GRBs) result from the collapse of a massive star into a black hole. The collapse releases so much energy that it rips the star's outer layers apart as a supernova explosion. Sometimes during the collapse to a black hole, the blast releases extremely high-energy jets of particles and radiation from the center; if one of these jets points toward Earth, astronomers see a GRB. ASTRONOMY: ROEN KELLY

14.3.2 Non-collapsars: short gamma ray bursts

Short GRBs are also cosmological in origin, and they show an afterglow emission similar to that of the long GRBs but less luminous. Lacking an association to a precursor supernova and given the short duration (down to tens of milliseconds), it is believed that the progenitors of the short GRBs are not massive stars but compact systems. Hence, short GRBs are considered to result from the merger of compact object binaries, two neutron stars (NS-NS) or a neutron star and a black hole (NS-BH) [479, 480]. Evidence of collimated emission is obtained from the study of spectral breaks in the light curves. Figure 14.9 illustrates stages in the merger of two neutron stars.

First Cosmic Event Observed in Gravitational Waves and Light

Colliding Neutron Stars Mark New Beginning of Discoveries

Collision creates light across the entire electromagnetic spectrum.
Joint observations independently confirm Einstein's General Theory of Relativity, help measure the age of the Universe, and provide clues to the origins of heavy elements like gold and platinum
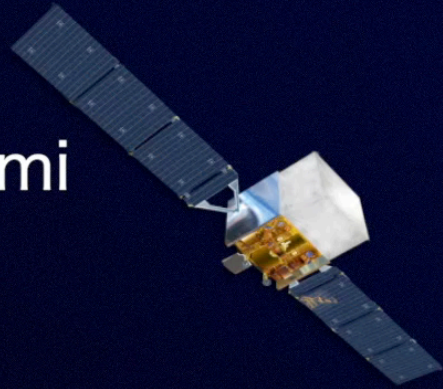
Gravitational wave lasted over 100 seconds

On August 17, 2017, 12:41 UTC, LIGO (US) and Virgo (Europe) detect **gravitational waves from the merger of two neutron stars**, each around 1.5 times the mass of our Sun. This is the first detection of spacetime ripples from neutron stars.
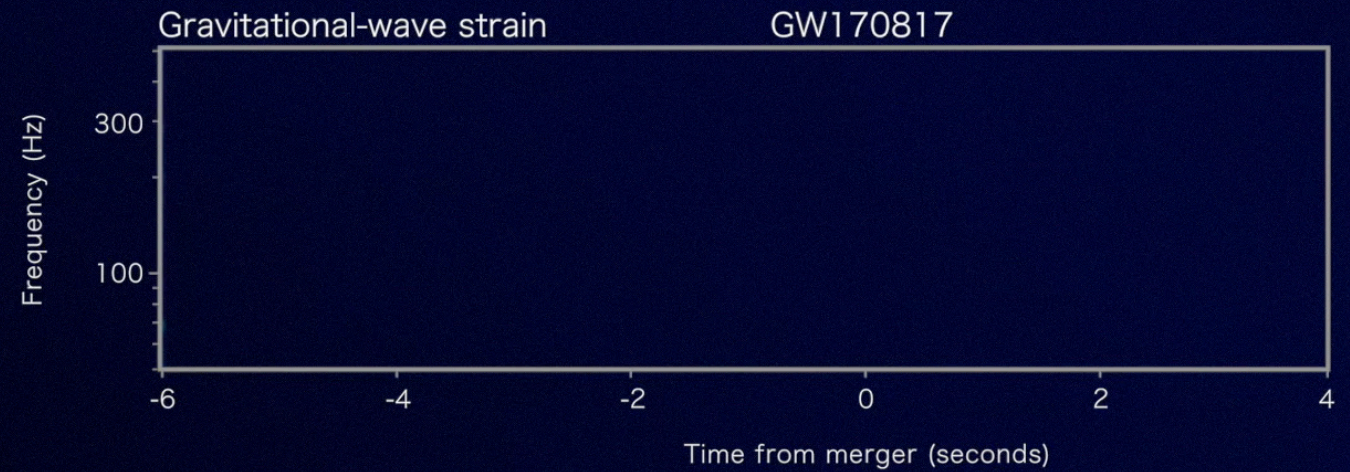
Within two seconds, NASA's Fermi Gamma-ray Space Telescope **detects a short gamma-ray burst** from a region of the sky overlapping the LIGO/Virgo position. Optical telescope observations pinpoint the origin of this signal to NGC 4993, a galaxy located 130 million light years distant.

LIGO Georgia Tech | Center for Relativistic Astrophysics College of Sciences NSF

Fermi

LIGO

Gamma rays, 50 to 300 keV   GRB 170817A

Counts per second

1,500 –

1,000 –

500 –

Gravitational-wave strain   GW170817

Frequency (Hz)

300 –

100 –

-6   -4   -2   0   2   4
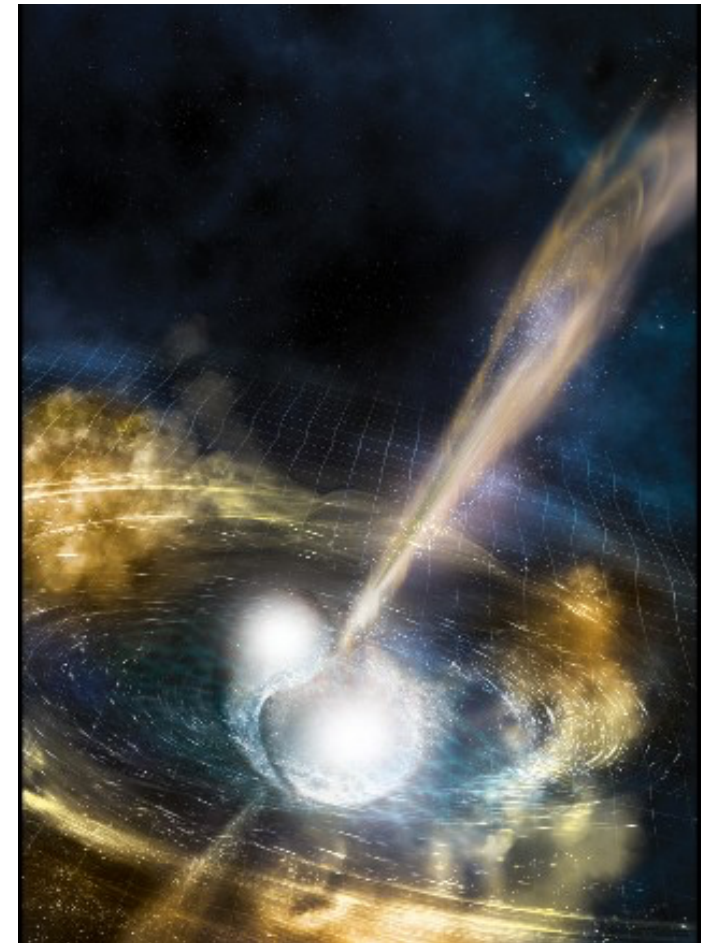
Time from merger (seconds)

Kilonova

A kilonova is a transient astronomical event

merging of NS-NS or NS-BH

—> short GRBs + gravitational waves

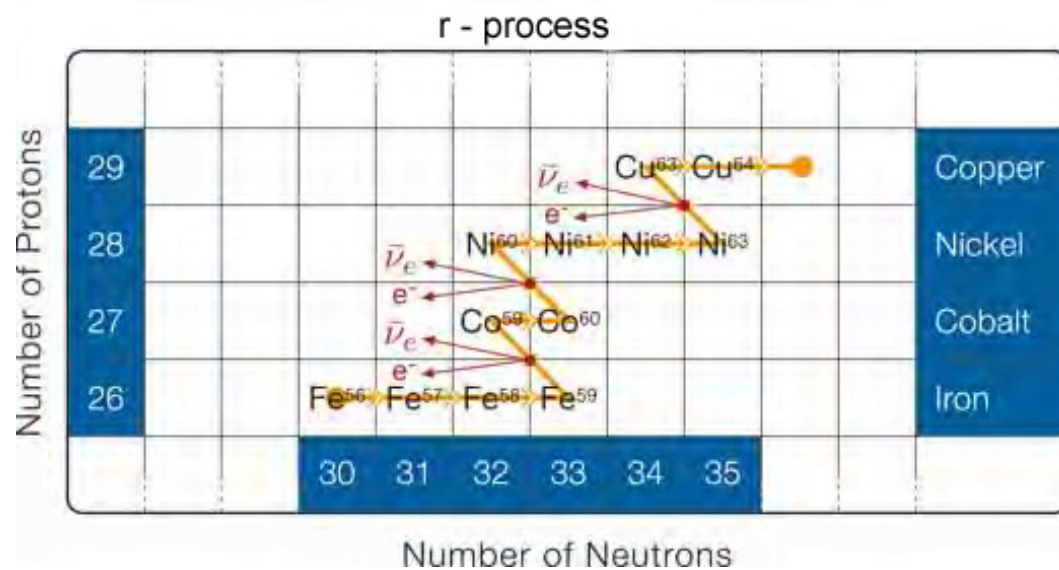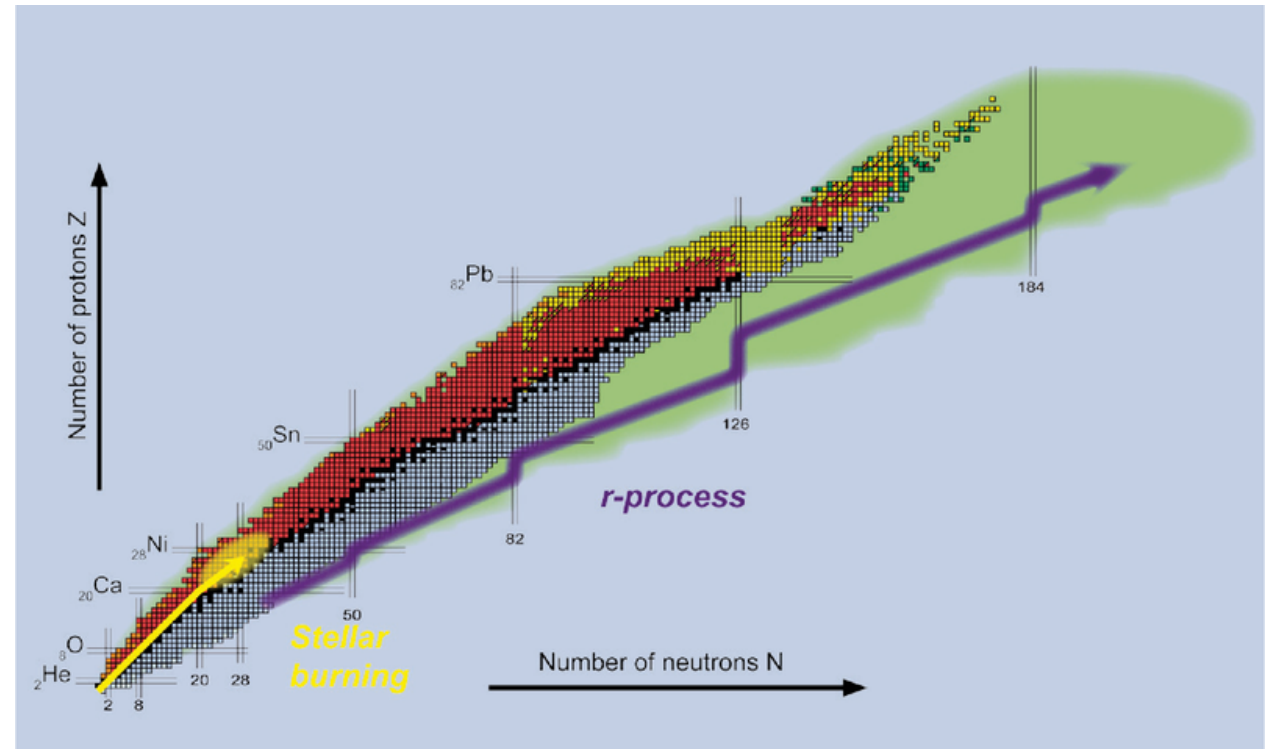—> strong electromagnetic radiation due to radioactive decay of r-process nuclei (heavy nuclei)

r-process

rapid neutron capture process

nucleosynthesis of atomic nuclei heavier than iron

very fast neutron capture, faster then beta decay

Gamma-Ray Bursts (GRBs): The Long and Short of It

Long gamma-ray burst
(>2 seconds' duration)

A red-giant star collapses onto its core....

...becoming so dense that it expels its outer layers in a supernova explosion.

Jet

Torus

Gamma rays

Short gamma-ray burst
(<2 seconds' duration)

Stars* in a compact binary system begin to spiral inward....

...eventually colliding.

The resulting torus has at its center a powerful black hole.
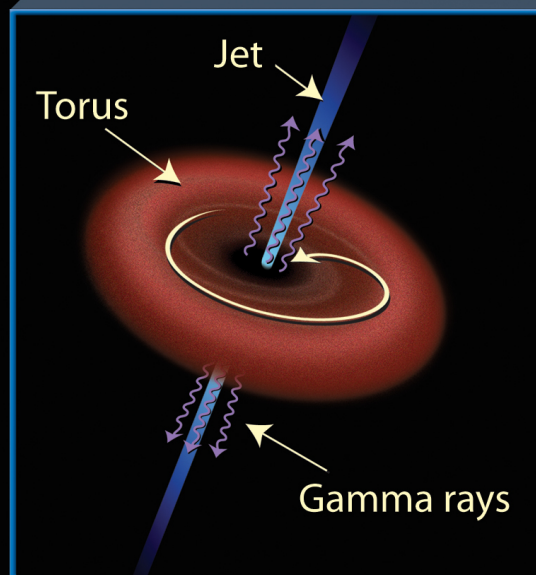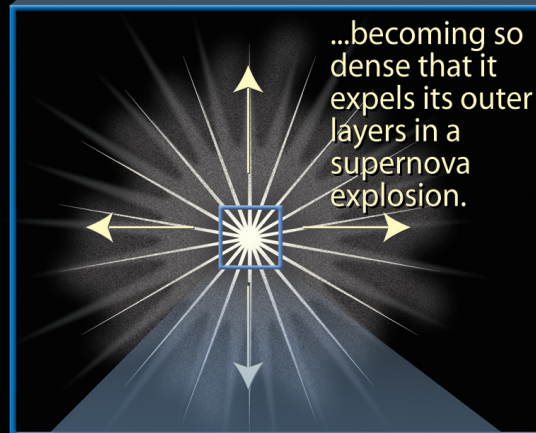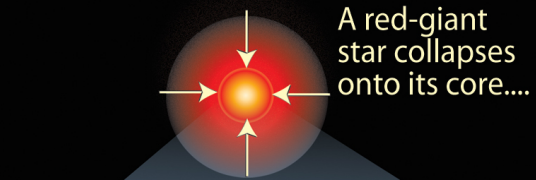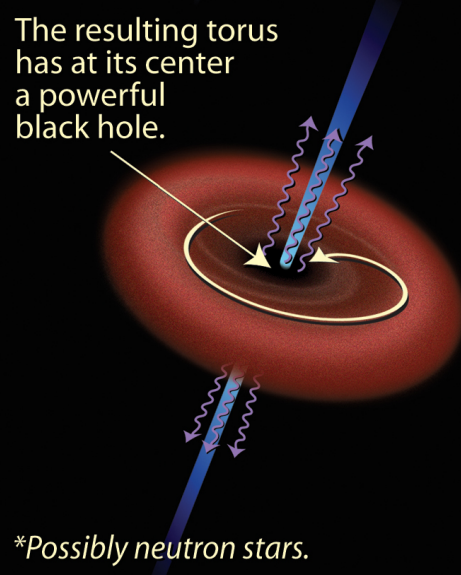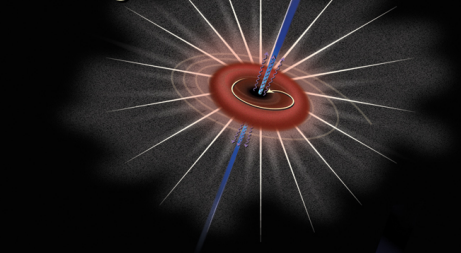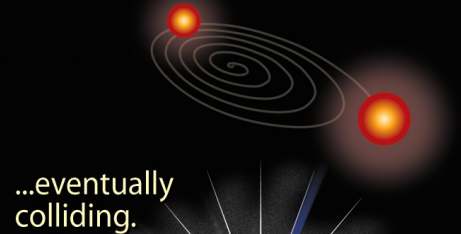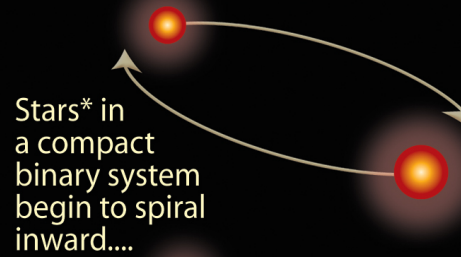
Possibly neutron stars.

14.3.3 Physical processes in gamma ray bursts

The physics of the GRB prompt emission is still not understood in full detail. The primary uncertainties concern: whether the composition of the ejecta are matter (baryon) dominated or electromagnetically dominated (Poynting flux); whether the energy dissipation is via internal or external shocks; and whether the radiative mechanisms are synchrotron, synchrotron self-Compton or Comptonization of thermal photons. For reviews we refer to [485, 771].

The spectral analyses of many GRBs shows that the emission is non-thermal and follows the empirical "Band" function [486], a double broken power law

$$N_E(E) \propto \begin{cases} E^\alpha \exp(-E/E_0) & E < E_0 \\ E^\beta & E > E_0 \end{cases} \qquad (14.28)$$

with the parameters $\alpha > \beta$ and E_0 which vary from burst to burst. Typical values are $\alpha \approx -1$ and $\beta \approx -2$. Although the spectrum of GRBs varies strongly from burst to burst, the fact that the Band function can explain the majority of the spectra implies a possible common physical origin of the burst emission. The Band function can describe both thermal and non-thermal processes, but the physical origin is not yet understood. Relativistic shocks are formed which contribute to the acceleration of particles from the plasma. Shocks can be *external* if they occur in interaction with the interstellar material or *internal* if in shells formed in the GRB itself. Internal shock scenarios [487] are more powerful and therefore more interesting for the topic of high-energy emission.

Discussion: In her review [450], Julia Becker Tjus describes the three phases in which neutrinos could be produced in GRBs. In the precursor phase (dark area in Figure 14.10), calculations [493, 494] predict the main neutrino signal to extend up to several TeV. In the afterglow phase, ultra-high-energy cosmic rays may be present to interact and photo-produce neutrinos of very high energy, $\sim$EeV [495]. During the main phase (medium grey region in Figure 14.10), the neutrino spectrum mirrors the Band spectrum of the target photons [492], and neutrinos in the 100 TeV range and somewhat above are predicted. This is a consequence of the importance of the Δ-resonance in photo-pion production (see Figure 4.22). Since the neutrino energy is proportional to the energy of the proton that produces it ($E_\nu \sim 0.05 \times E_p$), representing the cross section by a delta function

at the Δ resonance leads to the condition $E_\gamma \cdot E_\nu = $ const. Lower-energy neutrinos are produced from interactions with higher-energy photons (spectral index $\beta \approx -2$), while higher-energy neutrinos are produced from the lower-energy part of the photon distribution with spectral index $\alpha \approx -1$.
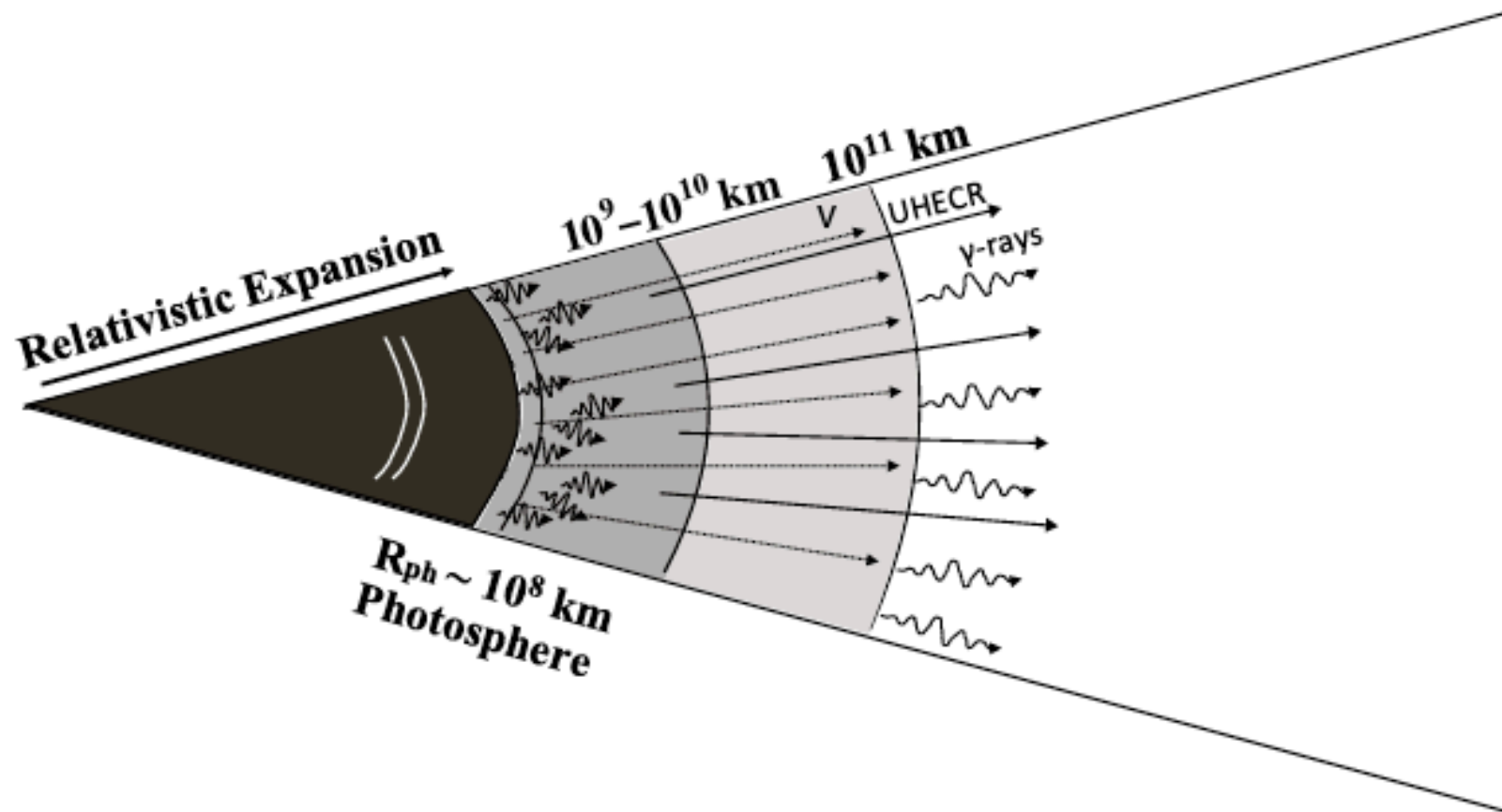
Figure 14.10 Schematic illustration of a GRB: the radiation dominated phase is represented in dark grey and it is followed by progressively more transparent phases. Following [491] high-energy neutrinos, ultra-high-energy cosmic rays (UHECR) and γ-rays are emitted at different radii.

The paper of Bustamante et al. [491] follows the neutrino production through the evolution of the burst to identify the distances from the explosions at which neutrinos, cosmic rays and γ-rays emerge. Their results are shown in Figure 14.11. The detailed calculation of Globus et al. [497] considers the acceleration of nuclei in GRBs in addition to protons. This model has interesting consequences for the origin of UHECR, which we discuss in Chapter 17.
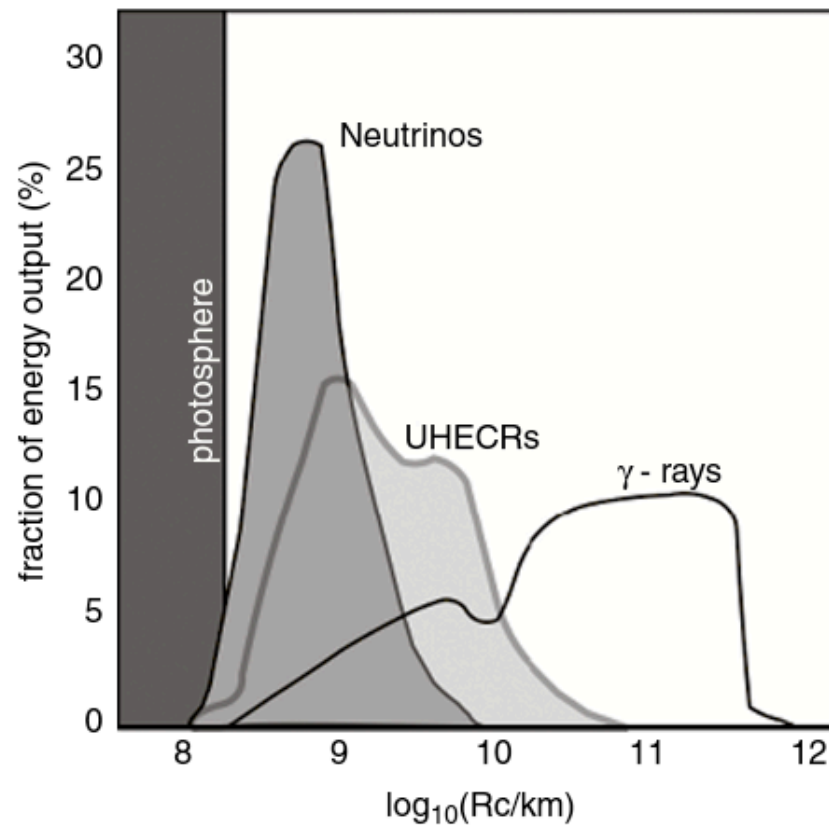
Figure 14.11 Figure modified from [491]: Fraction of the energy dissipated in prompt γ-rays, neutrinos and UHECR beyond the photosphere at different collision radius.

lecture 10
Extragalactic propagation of cosmic rays
Gaisser chapter 10

In this chapter we discuss the energy loss of protons, nuclei and photons propagating over extragalactic distances and the magnetic deflection of the charged particles. Energy loss processes are always linked to the production of secondary particles, such as gamma rays and neutrinos. The fluxes of these secondary particles can provide very important clues on the accelerated particles and the structure of the sources.

The most important interaction target for particles propagating over extragalactic distances is the cosmic microwave background (CMB). The energy spectrum is that of black body radiation with $T = 2.725\,$K, corresponding to an energy of $k_B T = 2.35 \times 10^{-4}\,$eV. The photon density is given by

$$\frac{dN_\gamma}{dV\,d\epsilon} = n_\gamma(\epsilon) = \frac{\epsilon^2}{\pi^2(\hbar c)^3(e^{\epsilon/k_B T} - 1)}. \qquad (10.1)$$

Integrated over photon energy ϵ we have 412 photons per cm^3 in our current cosmological epoch (redshift $z = 0$). Other important target photon fields are the infrared background and the universal radio background.

Soon after the discovery of the microwave background, Greisen [306] and Zatsepin and Kuzmin [307] realized that these photons make the universe opaque to protons and nuclei of very high energy (GZK effect). The energy threshold for pion production through $\gamma\, p \to \pi^0\, p$ follows from

$$s_{\text{th}} = (m_p + m_{\pi^0})^2$$

$$= m_p^2 + 2E_{\text{th}}\,\epsilon\,(1 - \beta_p \cos\theta) = m_p^2 + 2m_p\,\Gamma\,\epsilon\,(1 - \beta_p \cos\theta) \quad (10.2)$$

$$= m_p^2 + 2\epsilon'_{\text{th}}\, m_p. \quad (10.3)$$

As usual, we have for the proton energy and momentum $E = m_p\,\Gamma$ and $p = m_p\,\beta_p\,\Gamma$. Eq. 10.2 is written for the CMB rest frame with θ being the angle between the photon and the proton momenta and E_{th} the proton threshold energy. We obtain $E_{\text{th}} \sim 7 \times 10^{19}$ eV in the lab system for a head-on collision with a CMB photon of $\sim 10^{-3}$ eV. Protons with an energy greater than $\sim 7 \times 10^{19}$ eV undergo pion production with photons of the CMB and lose energy until they fall below the particle production threshold. In the proton rest frame (10.3) we have for the photon energy $\epsilon'_{\text{th}} \approx 145$ MeV; see also Figure 4.22.

Electromagnetic production of e^+e^- pairs, often referred to as Bethe–Heitler pair production, is another important energy loss process. With $s_{\text{th}} = (m_p + 2m_e)^2$, the energy threshold is $E_{\text{th}} \sim 6 \times 10^{17}$ eV. At the same time, the energy loss per produced e^+e^- pair is much smaller than in pion production.
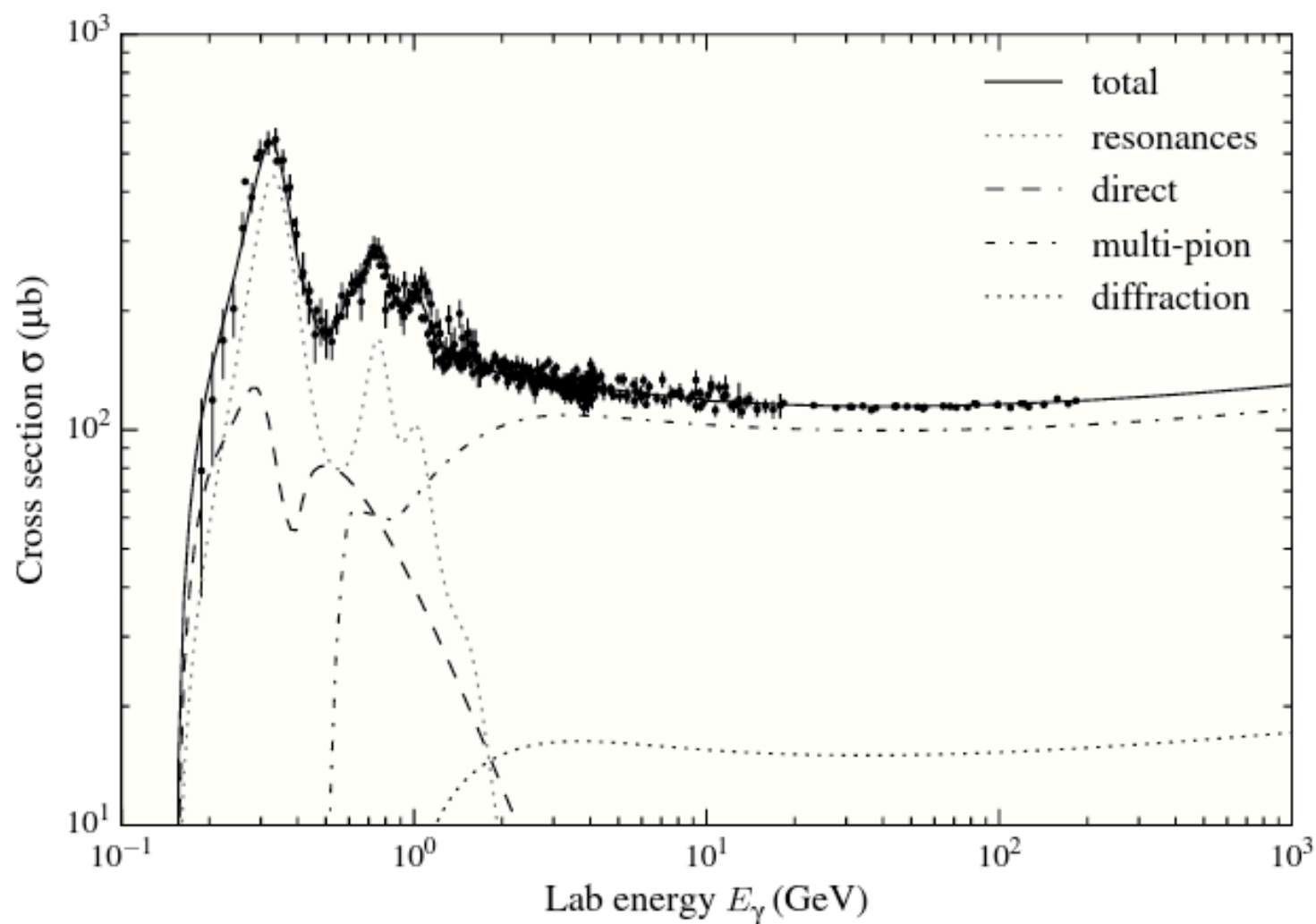
Figure 4.22 Total γ-p cross section as function of the photon energy E_γ in the lab system with the proton at rest. Four different components contributing to the hadronic cross section of photons are shown, the direct component (the photon produces directly a pion, Primakoff effect), resonance production (sum of eight individual resonances), and multipion and diffractive interactions (inelastic and elastic scattering of vector mesons) [138]. The cross section data are taken from the PDG compilation [10].

10.1 Energy loss for protons and neutrons

We first calculate the interaction rate of a particle propagating through the CMB. To avoid having to transform the CMB density to the proton rest frame to be able to apply Eq. 4.4 we use the general definition of the interaction rate as given in Eq. A.19. It differs from the cross section defined for a particle at rest by the factor $(1 - \vec{\beta}_a \cdot \vec{\beta}_b)$ with $c\,\vec{\beta}_{a/b}$ being the velocity vectors of the particles a and b. This factor is unity if one of the particles is at rest. Setting the density of the proton to $n_p(E) = \delta(E - E_p)$, the interaction rate is given by

$$\frac{dN_{\text{int}}}{dt} = \int c\,(1 - \beta_p \cos\theta)\,\frac{1}{4\pi}\,n_\gamma(\epsilon)\,\sigma(\epsilon')\,d\Omega\,d\epsilon, \qquad (10.4)$$

where we have added an integration over the angle of the photons and used the isotropy of the CMB to write

$$\frac{dN_\gamma}{d\epsilon\,dV\,d\Omega} = \frac{1}{4\pi}n_\gamma(\epsilon). \qquad (10.5)$$

The photon–proton cross section $\sigma(\epsilon')$ is shown in Figure 4.22 as a function of the photon energy ϵ' in the proton rest frame.

The photon energies in the two reference frames are related by a Lorentz transformation with the Lorentz factor Γ. Without having to apply this transformation explicitly we obtain from Eqs. 10.2 and 10.3

$$\epsilon' = \Gamma \epsilon \left(1 - \beta_p \cos\theta\right). \tag{10.6}$$

We then use this relation to replace the factor $(1 - \beta_p \cos\theta)$ by $\epsilon'/(\Gamma \epsilon)$ in (10.4) and apply the transformation

$$d\epsilon' = -\Gamma \epsilon \beta_p \, d\cos\theta \tag{10.7}$$

to obtain after integration over the azimuth

$$\frac{dN_{\text{int}}}{dt} = \frac{c}{2\Gamma^2} \int_{\epsilon'_{\text{th}}}^{\infty} \epsilon' \, \sigma(\epsilon') \int_{\epsilon'/2\Gamma}^{\infty} \frac{n_\gamma(\epsilon)}{\epsilon^2} \, d\epsilon \, d\epsilon'. \tag{10.8}$$

In the last step we have used $\beta_p \approx 1$. Requiring a physical value of $0 \leqslant 1 - \cos\theta \leqslant 2$ gives the lower limit on the integral over the energy ϵ.

The next step is to insert the CMB density (10.1) and carry out the integral over the photon energy ϵ. By changing variables from ϵ to $y = e^{\epsilon/k_B T} - 1$, we get an integral of the form $\int dy/[y(y+1)] = \int dy[1/y - 1/(y+1)]$, and Eq. 10.8 becomes

$$\frac{dN_{\text{int}}}{dt} = \frac{c\,k_B\,T}{2\pi^2(\hbar c)^3 \Gamma^2} \int_{\epsilon'_{\text{th}}}^{\infty} \epsilon'\,\sigma(\epsilon') \left\{ -\ln\left[1 - \exp\left(-\frac{\epsilon'}{2\Gamma k_B T} \right) \right] \right\} d\epsilon'. \quad (10.9)$$

After having calculated the interaction rate it is straightforward to derive the energy loss length by assuming that, in each interaction, the proton (or neutron) loses on average a fraction $f(\epsilon')$ of its energy

$$f(\epsilon') = \left\langle \frac{E_{\text{in}} - E_{\text{out}}}{E_{\text{in}}} \right\rangle = \frac{1}{\sigma(\epsilon')} \int (1-x)\frac{d\sigma(\epsilon')}{dx}\, dx, \quad (10.10)$$

with $x = E_{\text{out}}/E_{\text{in}}$ and E_{in} and E_{out} being the nucleon energies before and after the interaction.

The energy fraction lost per interaction is called *inelasticity*. Directly at the production threshold, i.e. the final state particles are at rest in CMS, the inelasticities for pion production and Bethe–Heitler pair production are given by the masses of the particles

$$f_\pi(\epsilon' \approx 145\,\text{MeV}) = \frac{m_{\pi^0}}{m_p + m_{\pi^0}} \approx 0.125, \qquad (10.11)$$

$$f_{e^+e^-}(\epsilon' \approx 1\,\text{MeV}) = \frac{2m_e}{m_p + 2m_e} \approx 10^{-3}. \qquad (10.12)$$

At higher energy we need to know the particle distributions in the final state. The inelasticity of photopion production increases slowly with energy from 0.125 to ~ 0.5 due to the increasing number of produced secondary particles. The mean inelasticity, already averaged over the contributing photon energies, is shown in Figure 10.1. In the proton energy range of relevance the mean inelasticity is about $0.15 - 0.2$. In contrast, the inelasticity of e^+e^- pair production falls with energy like a power law reaching 6×10^{-5} at $\epsilon' = 100\,\text{MeV}$; see [308] for a detailed discussion and references.
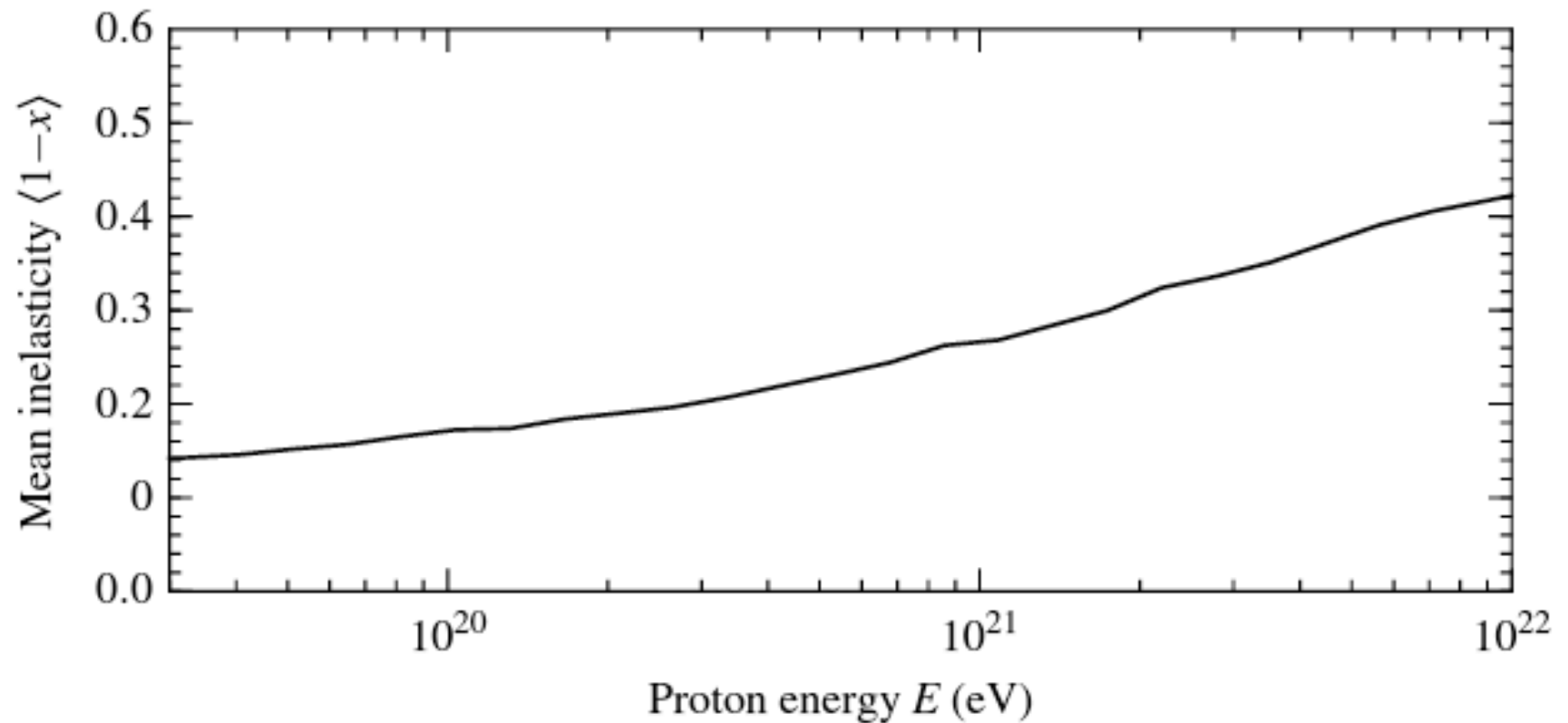
Figure 10.1 Mean inelasticity of hadronic proton interactions with photons of the CMB. The curve has been calculated using the dedicated Monte Carlo generator SOPHIA [138].

Putting all together, the fractional energy loss rate for an arbitrary background photon field and energy loss process is given by

$$\frac{1}{E}\frac{dE}{dt} = -\frac{c}{2\Gamma^2}\int_{\epsilon'_{th}}^{\infty}\epsilon'\,f(\epsilon')\,\sigma(\epsilon')\int_{\epsilon'/2\Gamma}^{\infty}\frac{n_\gamma(\epsilon)}{\epsilon^2}\,d\epsilon\,d\epsilon'. \qquad (10.13)$$

To understand the energy loss as a function of distance one defines the energy loss length

$$l_{loss} = -c\left(\frac{1}{E}\frac{dE}{dt}\right)^{-1} = -E\frac{ds}{dE}. \qquad (10.14)$$

The evolution of the particle energy along a trajectory is then given by

$$\frac{dE}{ds} = -\frac{E}{l_{loss}}. \qquad (10.15)$$

The energy loss length for the CMB and the individual contributions due to pion and e^+e^- pair production are shown in Figure 10.2. The adiabatic energy loss due to the expansion of the universe is given by the Hubble constant (see Appendix A.11)

$$\frac{1}{E}\frac{dE}{dt} = -H_0. \qquad (10.16)$$
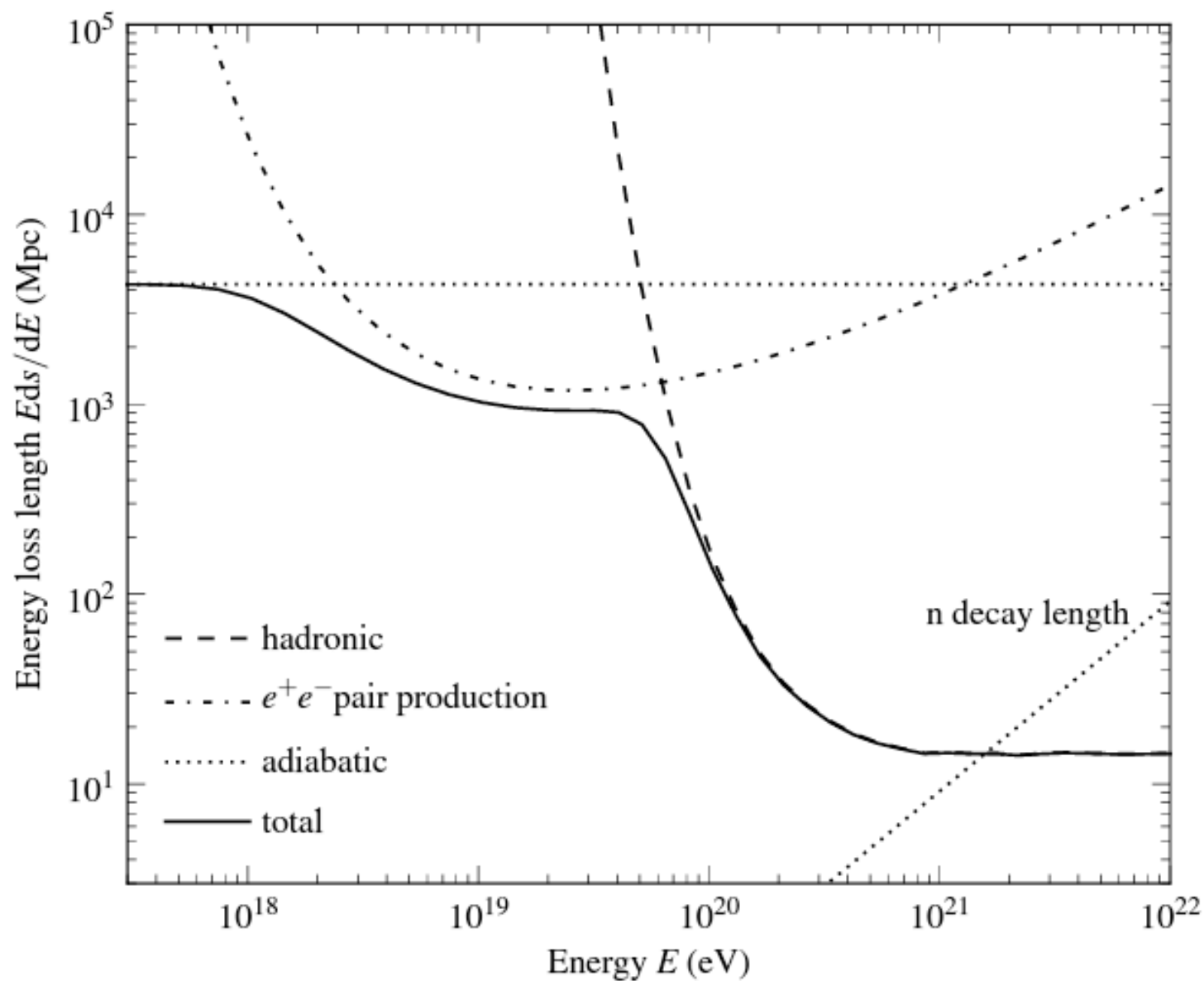
Figure 10.2 Energy loss length for protons in the CMB at redshift $z = 0$. Given are the total energy loss length and the contributions from e^+e^- (Bethe–Heitler) pair production, hadronic production of pions, and expansion of the universe ($H_0 = 70\,\text{km/s/Mpc}$). In addition the decay length of neutrons is shown.

Discussion: Replacing the cross section by a box function centered at the energy of the Δ resonance, various analytic approximations can be derived for the threshold behavior of the energy loss length due to interaction with the CMB. For example, Taylor gives [309]

$$l_{\text{loss}}(E) = \frac{l_0}{e^{-x}(1 - e^{-x})},$$
(10.17)

where $l_0 = 5\,\text{Mpc}$ and $x = 10^{20.53}\,\text{eV}/E$. And an approximation due to Dermer [310] is

$$l_{\text{loss}}(E) = \frac{13.7\,\text{Mpc}}{e^{-y}(1 + y)},$$
(10.18)

with $y = 4 \times 10^{20}\,\text{eV}/E$.

The difference in the energy loss length of protons and neutrons is very small. Neutrons, however, propagate without deflection by magnetic fields. Therefore we also show the neutron decay length in Figure 10.2. The interaction length due to photopion production is about five times shorter than the energy loss length, i.e. about 4 Mpc around 10^{21} eV. At this energy, the interaction length and decay length of neutrons are comparable and neutrons tend to interact before decaying.

The energy loss length does change with redshift. The temperature of the CMB scales as $T(z) = T_0(1 + z)$ and the density of photons as $n_\gamma(z) = n_{\gamma,0}(1 + z)^3$. Hence we have

$$l_{\text{loss}}(E, z) = (1 + z)^{-3} l_{\text{loss}}((1 + z)E, z = 0). \tag{10.19}$$

To calculate the expected proton spectrum on Earth one has to integrate over the contribution of all sources. For clarity we write the expression for identical sources and without cosmological corrections

$$\frac{dN_{\text{obs}}}{dE\, dt\, dA} = \int \frac{dN_{\text{inj}}}{dE_{\text{src}}\, dt_{\text{src}}} \frac{dn_{\text{src}}}{dV} \left(\frac{\partial E_{\text{src}}}{\partial E}\right) \frac{1}{4\pi R^2} R^2 dR\, d\Omega, \tag{10.20}$$

where the first factor is the number of particles injected per unit time by a single source, the second factor describes the density of sources, and the Jacobian in brackets accounts for the energy loss of the particles.

Often the number of sources per unit comoving volume is written as $\mathrm{d}n_{\mathrm{src}}/\mathrm{d}V = n_0 \mathcal{H}(z)$ where, for example,

$$\mathcal{H}(z) = \begin{cases} (1+z)^m & : \quad z < 1.9 \\ (1+1.9)^m & : \quad 1.9 < z < 2.7 \\ (1+1.9)^m \exp\{(2.7-z)/2.7\} & : \quad z > 2.7 \end{cases} \qquad (10.21)$$

parametrizes the evolution of the sources, with m being a model parameter. Accounting for cosmological evolution and time dilation we can rewrite (10.20) with $R = c\,\mathrm{d}t$ and, see Appendix A.11,

$$c\,\mathrm{d}t = \frac{c}{H_0(1+z)}\left[\Omega_m(1+z)^3 + \Omega_\Lambda\right]^{-1/2}\,\mathrm{d}z = \eta(z)\,\mathrm{d}z \qquad (10.22)$$

as

$$\frac{\mathrm{d}N_{\mathrm{obs}}}{\mathrm{d}E\,\mathrm{d}t\,\mathrm{d}A\,\mathrm{d}\Omega} = \int \frac{\mathrm{d}N_{\mathrm{inj}}}{\mathrm{d}E_{\mathrm{src}}\,\mathrm{d}t_{\mathrm{src}}} \frac{\mathrm{d}n_{\mathrm{src}}}{\mathrm{d}V} \left(\frac{\partial E_{\mathrm{src}}}{\partial E}\right) \eta(z)\,\mathrm{d}z, \qquad (10.23)$$

where we have assumed a spatially flat universe.

As application of Eq. 10.23 we show in Figure 10.3 the proton spectrum on Earth for uniformly distributed sources that inject a proton spectrum $dN_{inj}/dE_{src} \sim E_{src}^{-\gamma}$. The energy losses lead to a suppression of high-energy particles, the so-called *GZK cutoff*. There is a direct correlation between the effective source volume and the energy of the particles in the spectrum. In particular, the highest energy part of the spectrum originates only from local sources, i.e. sources within the *GZK sphere* of $75 - 150$ Mpc radius.

Starting with a power-law injection spectrum of protons, the energy loss effect leads to the formation of a dip at the energy of the ankle (when plotted as $E^3 \, dN/dE$) and a suppression at the highest energies. The energy relation between the dip and the suppression as well as the complete spectral shape, which can be described by a universal modification factor [308, 312], is an inherent feature of this source model and gives a good qualitative description of flux measurements (see also discussion in Chapter 17).

The spectral feature seen at $E > 10^{20.5}$ eV, which is often referred to as *flux recovery*, is the result of performing the calculation for a continuous source density. The high-energy end of the spectrum depends on the location of the nearest sources as discrete injection points [313]. If there are no sources within ~ 20 Mpc of Earth that inject protons of such energies then we do not expect a flux recovery.
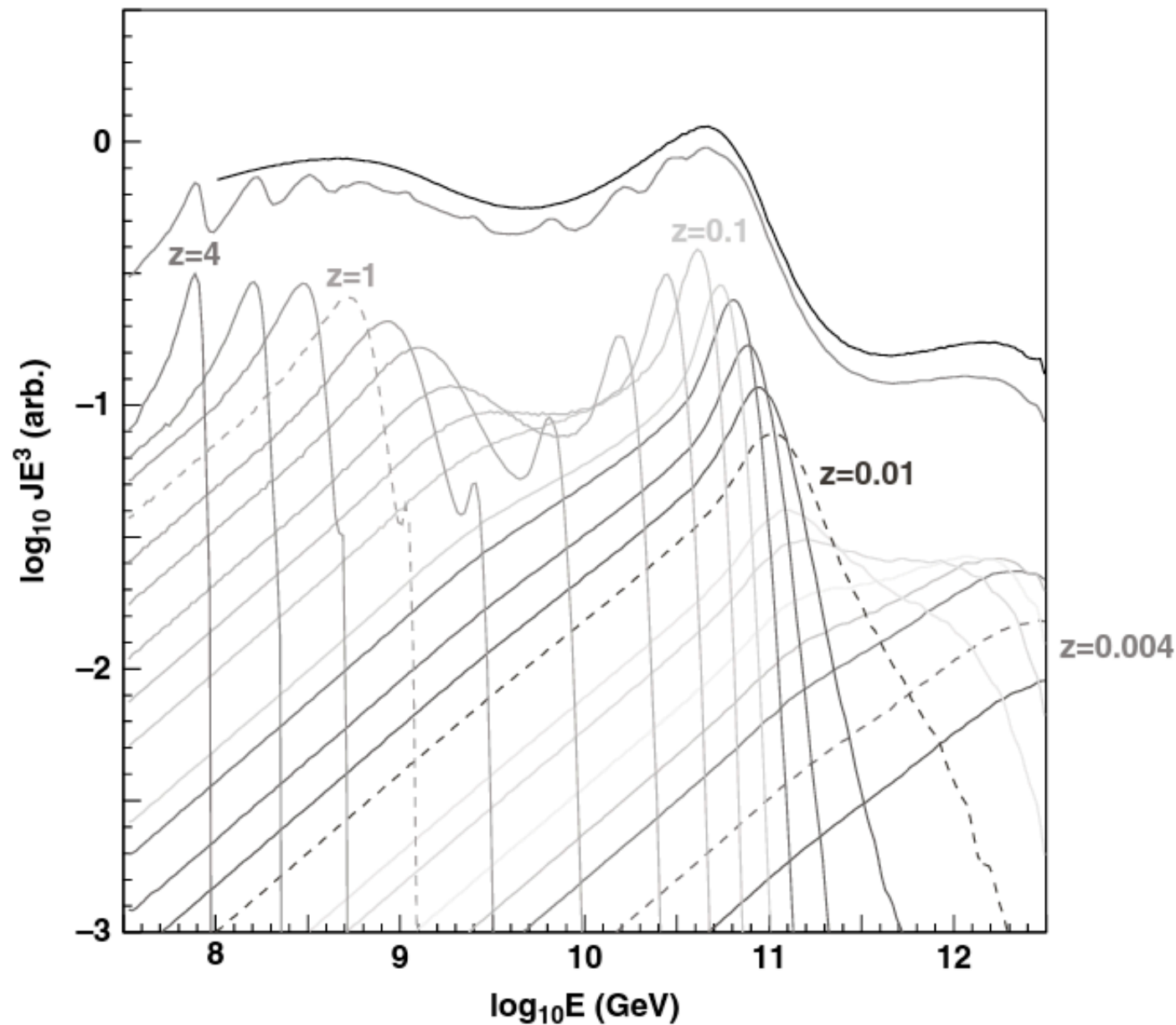
Figure 10.3 Expected energy spectrum on Earth for sources injecting protons with spectral index $\gamma = 2.38$ and a cosmological evolution parameter $m = 2.55$ for all redshifts. In addition, the contribution of sources at different distances and their sum is shown. (Douglas Bergman, private communication and [311])

10.2 Photodisintegration of nuclei

Photodisintegration is the dominant interaction process of ultra-high-energy nuclei propagating in the microwave background [314]. In addition to the CMB, also photons of the infrared background are important as interaction target [315].

The physics of photohadronic interactions is discussed in Section 4.5; here we recall only some important features of relevance to the following calculation. At low energy ($\epsilon' \lesssim 25 - 30 \, \text{MeV}$, ϵ' being the photon energy in the nucleus rest frame) the photon absorption cross section is mainly given by that of the giant dipole resonance (GDR). In the decay after absorbing a photon, the excited nucleus emits mainly a single neutron or proton, but sometimes also two nucleons. In the energy region between $30 \, \text{MeV} \lesssim \epsilon' \lesssim 145 \, \text{MeV}$ the absorption of photons leads to the emission of several nucleons. The number of emitted nucleons has a wide distribution with two-nucleon emission having the highest probability. At energies higher than $145 \, \text{MeV}$, the threshold for single pion production, photo-production interactions with single nucleons take place similar to interactions with free protons or neutrons. It is important to keep in mind that the energy per nucleon stays approximately constant in the lab system, i.e. the rest system of the CMB.

In analogy to the calculation (10.8) for protons, we can calculate the partial interaction rate with the target photon field

$$\frac{dN_{A,k}}{dt} = \frac{c}{2\Gamma^2} \int_0^\infty \epsilon' \, \sigma_k(A, \epsilon') \int_{\epsilon'/2\Gamma}^\infty \frac{n_\gamma(\epsilon)}{\epsilon^2} \, d\epsilon \, d\epsilon', \qquad (10.24)$$

where we consider only interactions $\gamma \, A \to (A - k) \, X$, in which the mass number of the parent nucleus is reduced to $A - k$ by the emission of k nucleons. The total interaction rate is then given by

$$\frac{dN_A}{dt} = \sum_{k \geq 1} \frac{dN_{A,k}}{dt}. \qquad (10.25)$$

With the single nucleon energy $E_{\text{nuc}} = \Gamma \, m_p$ being conserved in these interactions, the relative energy loss rate of the nucleus is

$$\frac{1}{E} \frac{dE}{dt} = \frac{1}{A} \frac{dA}{dt} = -\frac{1}{A} \sum_{k \geq 1} k \frac{dN_{A,k}}{dt}. \qquad (10.26)$$

The energy loss length of iron nuclei and the breakdown into different loss processes are shown in Figure 10.4. In contrast to proton propagation, the resulting loss length is a complex superposition of the contributions due to $e^+ e^-$ pair production, photodissociation, and pion photoproduction.
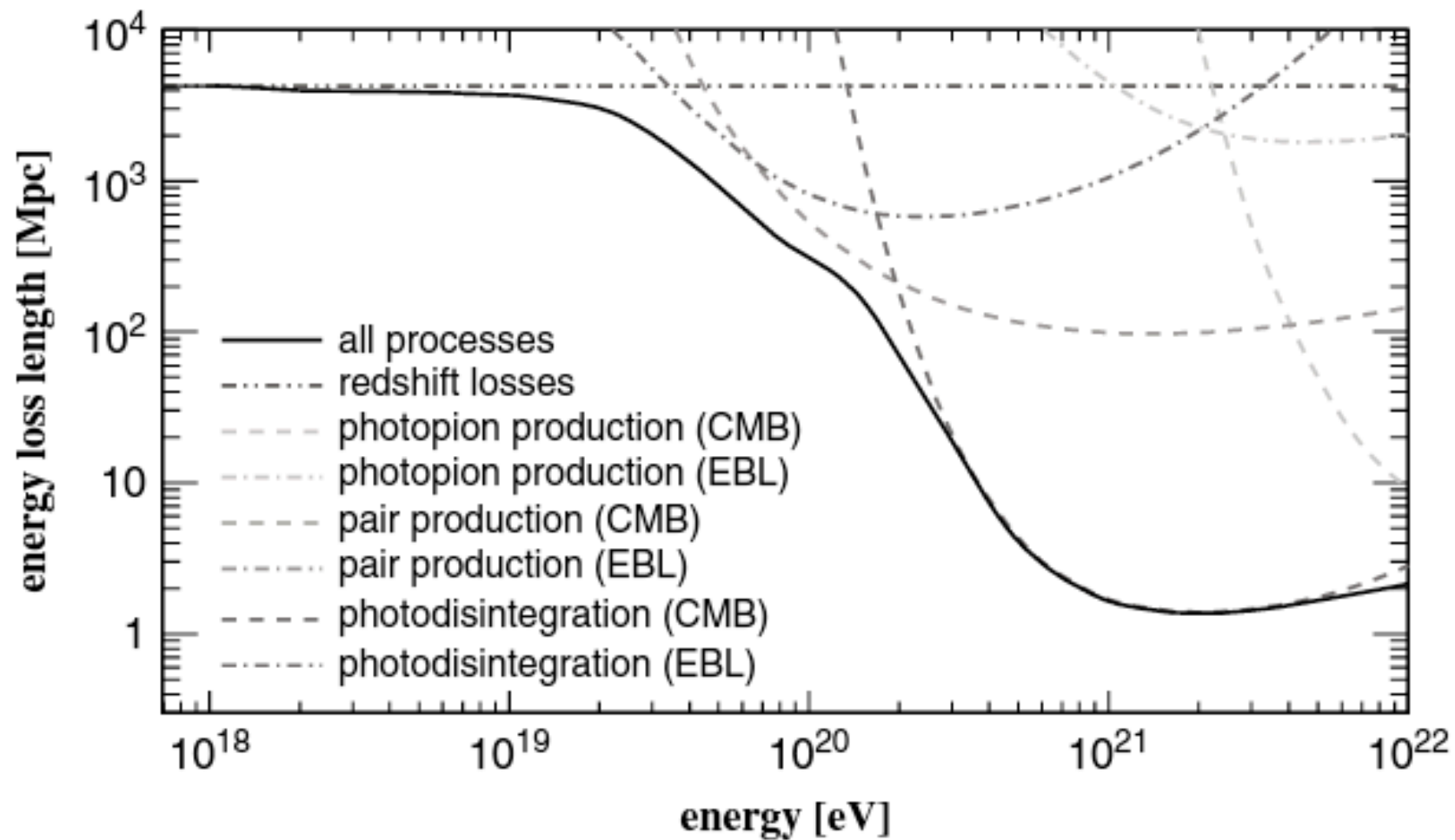
Figure 10.4 Energy loss length for iron nuclei calculated with CRPropa [316] using the model of Gilmore et al. [317] for the extragalactic background light (EBL). Shown are the contributions due to different interaction processes with CMB and EBL photons. From [185].

An important aspect is that, although the relative energy loss might be very small per interaction, the nucleus mass number changes with each interaction. The interaction cross section is for all nuclei the largest in the GDR range, corresponding to $\epsilon'_{GDR} \sim 15 - 25\,\text{MeV}$. In the rest frame of the CMB, the equivalent energy of the nucleus $E_{GDR} = A\,\Gamma_{GDR}\,m_p$ follows from

$$
\begin{aligned}
s &= (A\,m_p)^2 + 2\epsilon'_{GDR}\,A\,m_p \\
&= (A\,m_p)^2 + 2E_{GDR}\,\epsilon\,(1 - \beta\cos\theta) \\
&= (A\,m_p)^2 + 2\Gamma_{GDR}\,A\,m_p\,\epsilon\,(1 - \beta\cos\theta).
\end{aligned}
\tag{10.27}
$$

Thus, if a nucleus with mass number A has a Γ factor that allows for an efficient interaction with background photons, then this applies to all the daughter nuclei, too. The Lorentz factor for resonant interaction is independent of the mass number

$$
\Gamma_{GDR} = \frac{\epsilon'_{GDR}}{\epsilon\,(1 - \cos\theta)}.
\tag{10.28}
$$

Another consequence of these kinematic relations is that, for a given total energy, the thresholds for photodisintegration and pion production scale with the mass number A of the nucleus. For example, helium nuclei disintegrate already at an energy that is ~ 14 times lower than that for iron breakup. Therefore a mass-dependent change of the observed cosmic ray composition at the highest energies, which is similar to a Peters cycle but scaling with A instead of Z, could be the signature of nucleus interaction in radiation fields either in the sources or during extragalactic propagation; see discussion in Chapter 17. And, depending on the steepness of the injection spectrum, the secondary protons stemming from photodissociation can be an important part of the cosmic ray spectrum on Earth [318, 319].

Finally we want to note that, by coincidence, the effective suppression of a power-law injection spectrum due to energy loss effects is similar for protons and nuclei in the silicon to iron mass range at energies $E > 7 \times 10^{19}$ eV.

10.3 Secondary particle production

The interaction of ultra-high-energy protons and nuclei with photons of the background radiation leads to fundamentally different secondary particle spectra. Protons produce charged pions as secondaries, which decay and give rise to a neutrino flavor composition of

$$\nu_e : \nu_\mu : \nu_\tau = 1 : 2 : 0. \tag{10.29}$$

If the production is dominated by the single pion channel, as one would expect for a steep source spectrum, we can write explicitly

$$
\begin{aligned}
p\,\gamma \longrightarrow n\,\pi^+ &\longrightarrow n\,\mu^+\,\nu_\mu \\
&\longrightarrow n\,e^+\,\nu_e\,\nu_\mu\,\overline{\nu}_\mu \\
&\longrightarrow p\,e^-\,e^+\,\nu_e\,\overline{\nu}_e\,\nu_\mu\,\overline{\nu}_\mu,
\end{aligned} \tag{10.30}
$$

where we have included neutron decay in the last step. The decay chain shown here is not applicable in all calculations of secondary fluxes because secondary particles might lose energy or interact before decaying, depending on the environment in which the processes take place [320]. As a first estimate we can assume that all four secondary particles of the pion decay share the pion energy democratically, and with the pion energy being about 20% of that of the proton we obtain a typical neutrino energy of $E_\nu \sim 0.05\,E_p$. The only exception is the $\overline{\nu}_e$ from the neutron decay. It carries only a fraction of $\sim 10^{-5}$ of the neutron energy.

With this knowledge we can understand the basic features of the neutrino fluxes arising from the interaction of ultra-high-energy protons with photons of the CMB. These neutrinos are often called *GZK neutrinos* or *cosmogenic neutrinos* as they are the byproduct of the GZK effect. Assuming low density and weak magnetic fields, all secondary particles of these proton interactions decay without further energy losses.

The calculation of the flux of cosmogenic neutrinos is a straightforward application of Eq. A.19, similar to the calculation of the interaction rate. We can take advantage of the fact that, due to the GZK effect, protons fall below the particle production threshold within a propagation distance of ~ 200 Mpc and calculate for this distance range and a given proton source spectrum a generic neutrino source function. This source function has then to be properly re-scaled for different redshifts and serves as flux factor in Eq. 10.23, replacing the proton source flux, for integrating over all distances (for details see [321]).

The expected cosmogenic neutrino flux for a source spectrum $dN/dE \sim E^{-2}$ up to $10^{20.5}$ eV is shown in Figure 10.5. As expected, the ν_μ and $\overline{\nu}_\mu$ fluxes are identical. The shift of flux maximum from ν_e to $\overline{\nu}_e$ follows from the exceptional role of the neutron decay. The small flux of $\overline{\nu}_e$ around 10^{18} eV stems from secondary π^- of multi-pion production reactions.
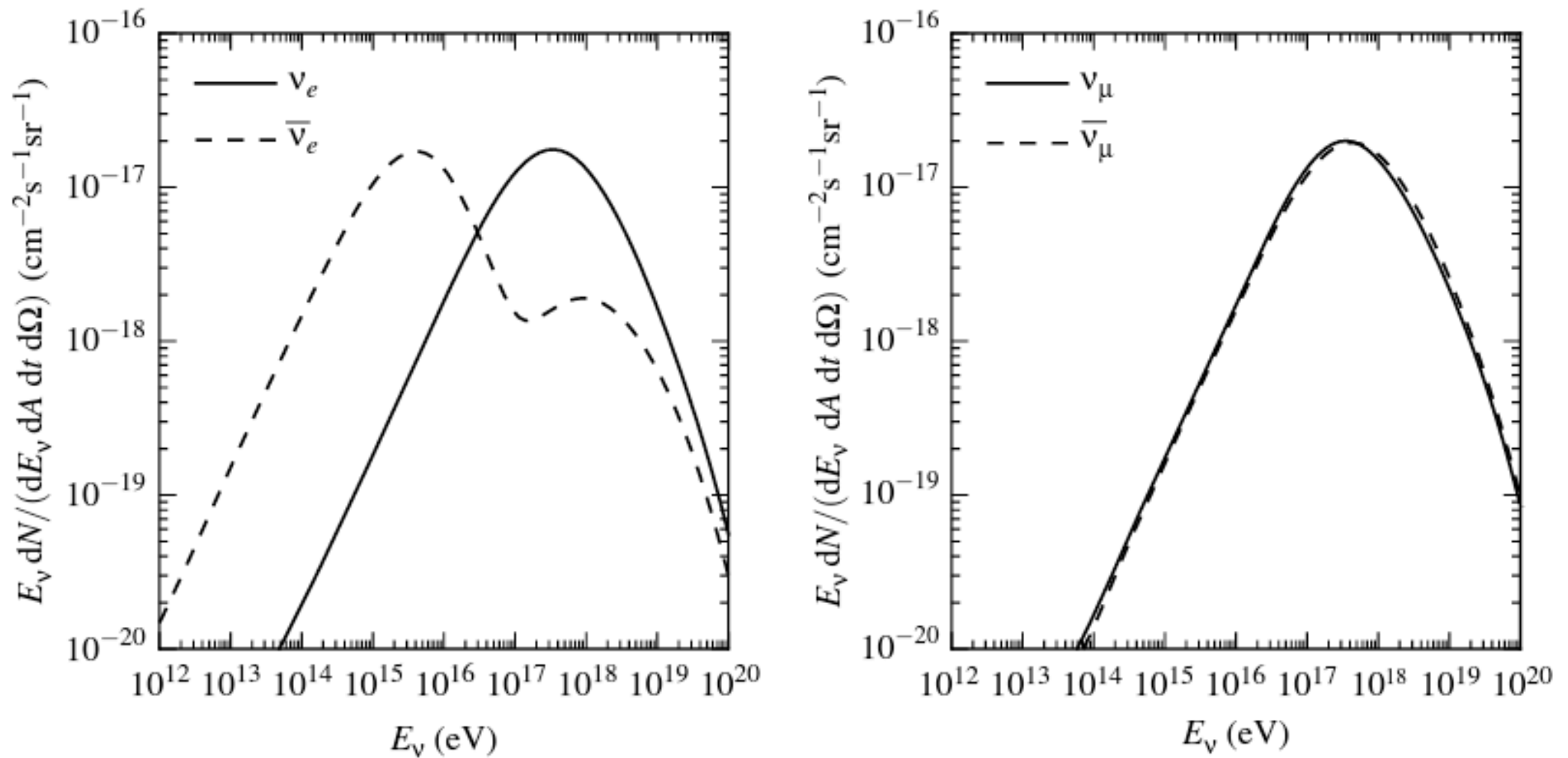
Figure 10.5 Flux of cosmogenic neutrinos from proton interaction with the microwave background [321].

If sources of ultra-high-energy cosmic rays inject only nuclei, the expected rate of cosmogenic neutrinos is drastically lower. With pion production being energetically disfavored, only neutron decay remains as a source process. The expected fluxes of neutrinos arising from proton and nuclei propagation are compared in Figure 10.6. The injected cosmic ray fluxes have been tuned to reproduce the all-particle flux measurements of the Telescope Array [325] and Auger [326] collaborations. Also shown is the flux of astrophysical neutrinos measured by IceCube [327] and upper limits from the Auger Observatory.

The proton flux at ultra-high-energy is a measure of the "cosmologically" local source population. In contrast, neutrinos propagate over cosmological distances and the neutrino flux is an integral measure of the source activity throughout the entire visible universe. Thus the neutrino flux is also sensitive to the source evolution with redshift.

With a 66% branching ratio the decay of a Δ^+ resonance produces a neutral pion, which in turn decays to two photons. The calculation of the corresponding photon fluxes is analogous to that of neutrino fluxes; see, for example, [328].
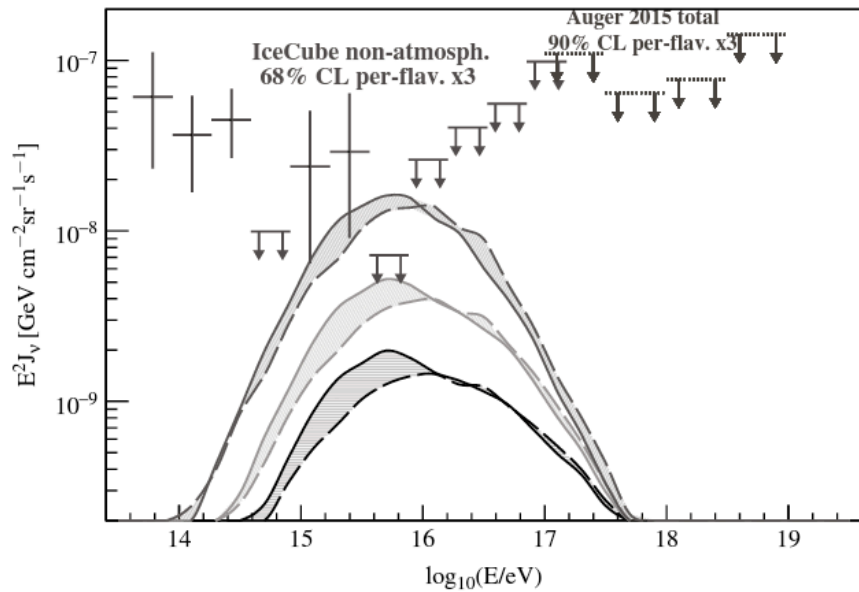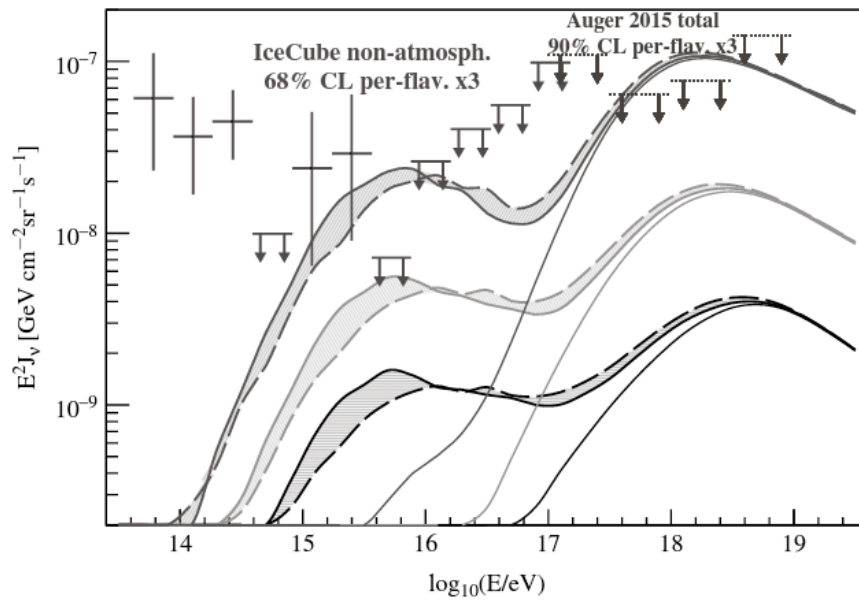
Figure 10.6 Neutrino flux predictions for two source models and different cosmological source evolution scenarios, from [322]. Top: neutrino fluxes if the all-particle flux of cosmic rays as measured by Telescope Array is described by a source model with only protons. Bottom: neutrino fluxes for a mixed composition model tuned to reproduce the flux and composition data of the Auger Observatory. In addition neutrino flux limits of IceCube and the Auger Observatory are shown. Each time three source evolution scenarios are shown: no evolution, evolution according to the star formation rate (SFR), and evolution according to AGNs (from bottom to top). The calculation was made with SimProp [323].

Discussion: A simple order-of-magnitude estimate of the injected photon flux due to proton interactions follows from the relation between charged and neutral pions in photoproduction. Let's assume the proton source function is

$$Q_p(E_p) = \frac{dN_p}{dE_p \, dV \, dt} = A \, E_p^{-s}, \tag{10.31}$$

with $s = 2$ for standard Fermi acceleration. In the limit of a single interaction with the CMB, the secondary neutrino yield is given by

$$Q_\nu(E_\nu) = \frac{dN_\nu}{dE_\nu \, dV \, dt} = \left(\int_0^1 (x_L)^{s-1} \frac{dN_\nu}{dx_L} \, dx_L \right) A \, E_\nu^{-s} = Z_{p\nu} \, Q_p(E_\nu), \tag{10.32}$$

where $Z_{p\nu}$ is the spectrum-weighted moment, or Z-factor, for neutrino production (see discussion in Sections 5 and 6). For an E^{-2} spectrum, this factor is the probability to produce a π^+ times the relative energy fraction given to the neutrino flavor we are interested in.

For example, we have $Z_{p\nu} = 0.33 \times 0.05$ for muon neutrinos (single flavor). The same calculation can be done for photons keeping in mind that $Z_{p\gamma} = 0.67 \times 0.2$. In general we can write

$$(E_\nu)^s \, Q_\nu(E_\nu) = Z_{p\nu} \, (E_\nu)^s \, Q_p(E_\nu) \tag{10.33}$$

$$(E_\gamma)^s \, Q_\gamma(E_\gamma) = Z_{p\gamma} \, (E_\gamma)^s \, Q_p(E_\gamma) \tag{10.34}$$

and obtain

$$Z_{p\gamma} \, (E_\nu)^s \, Q_\nu(E_\nu) = Z_{p\nu} \, (E_\gamma)^s \, Q_\gamma(E_\gamma), \tag{10.35}$$

for the relation between the photon and neutrino fluxes at production. And for $E_\gamma = E_\nu$ we have

$$\boxed{\frac{Q_\gamma(E)}{Q_\nu(E)} = \frac{Z_{p\gamma}}{Z_{p\nu}}.} \tag{10.36}$$

There is, however, an important difference between photons and neutrinos. High-energy photons produce e^+e^- pairs with background photons and are absorbed. The produced electrons undergo inverse-Compton scattering and produce synchrotron radiation, transferring the energy of the high-energy photons to photons in the energy range well below 10^{14} eV. The relevant length scales are shown in Figure 10.7.
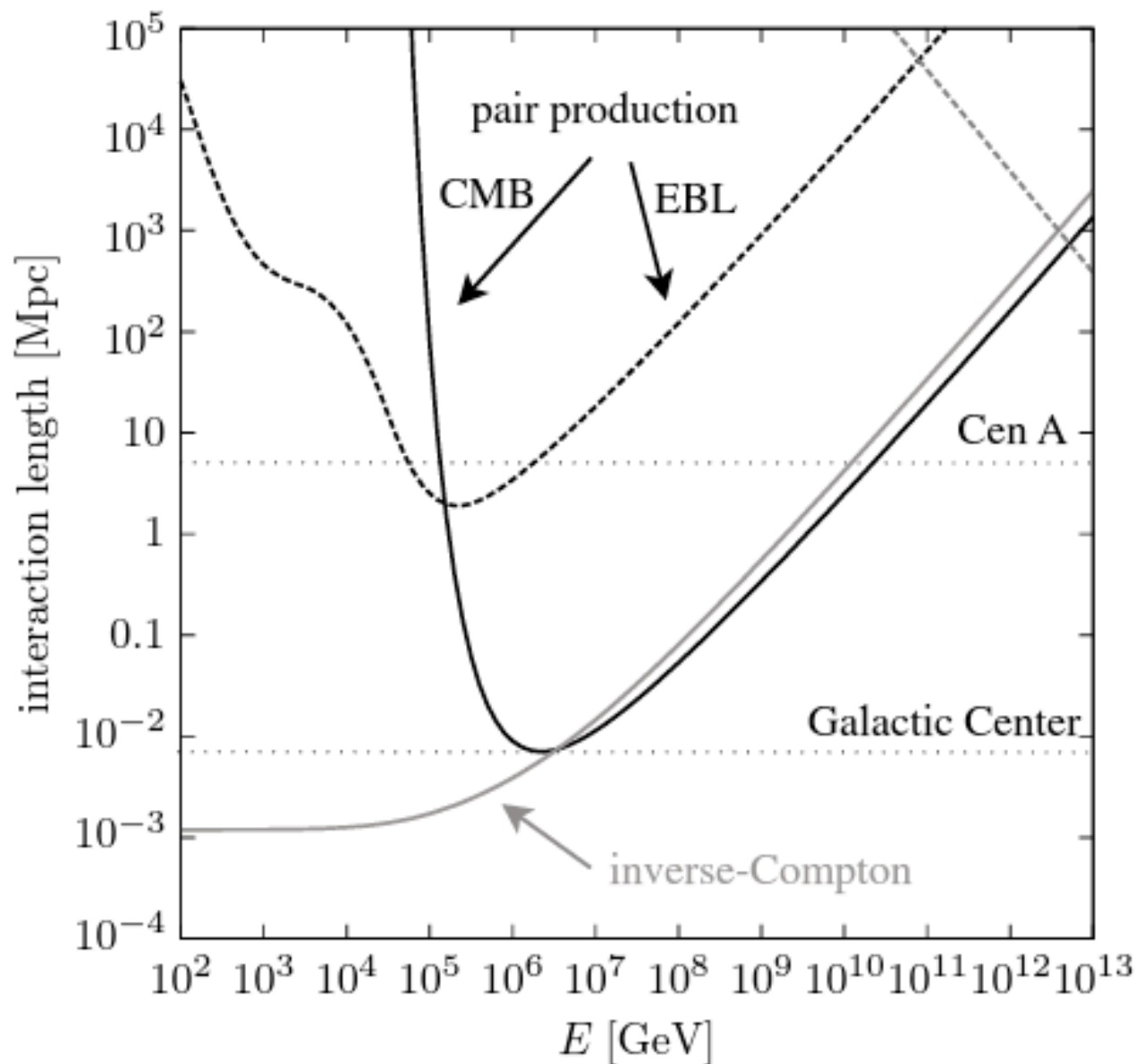
Figure 10.7 Length scales for $\gamma\gamma \rightarrow e^+e^-$ pair production and inverse-Compton scattering of photons with the CMB and EBL. The distances to the Galactic Center and the radio galaxy Cen A are marked for reference. From [324].

10.4 The role of magnetic fields

Extragalactic particles are deflected on their way to Earth by Galactic and extragalactic magnetic fields. The regular component of the local Galactic field is about $3\,\mu G$ and a Kolmogorov-type turbulent component of comparable size is expected. A widely used model of the Galactic field has been developed by Jansson and Farrar [329] by combining WMAP data with a very large set of Faraday rotation measurements. Simulations of proton trajectories through the Galactic magnetic field predict deflection angles of the order of $\sim 5°$ for 6×10^{19} eV as long as the trajectory does not come too close to the Galactic center [330, 331].

While there has been much progress in understanding the regular and turbulent components of the Galactic magnetic field [329, 332], little is known about extragalactic fields. Extragalactic magnetic fields on intergalactic scales vary in strength and coherence length over many orders of magnitude. They can be as large as 10^{-6} G with a coherence lengths of $l_c \sim 100\,\text{kpc}$ in galaxy clusters and are probably larger than 10^{-15} G, but also smaller than 10^{-9} G, in voids with a coherence scale of $l_c \sim 1\,\text{Mpc}$ [333]. Given these large uncertainties we will discuss here only some basic estimates for the expected deflection angles and corresponding time delays following Achterberg et al. [334], where the derivation can be found.

In the small angle approximation we have $\delta\theta \approx d/R_L$, where d denotes the propagation distance. The Larmor radius is given by

$$R_L = \frac{R}{B_\perp} = \frac{E}{Z\,e\,B_\perp},$$

(10.37)

with R being the particle rigidity and $B_\perp$ the magnetic field strength perpendicular to the particle trajectory. Using the coherence length l_{coh} one can show that the scalar diffusion coefficient $D_0 = (1/3)l_{\text{coh}}/R_L^2$ describes the random walk of two-dimensional small angle deflections.[1] Then the quadratic deflection angle relative to the line of sight to a source is given by

$$\langle\Delta\theta^2\rangle \approx \frac{4\,d\,l_{\text{coh}}}{9\,R_L^2}.$$

(10.38)

With $\theta_{\text{RMS}} = \sqrt{\langle\Delta\theta^2\rangle}$ we can write

$$\theta_{\text{RMS}} \approx 3.5° \left(\frac{Z\,B}{10^{-9}\,\text{G}}\right)\left(\frac{10^{20}\,\text{eV}}{E}\right)\left(\frac{d}{100\,\text{Mpc}}\right)^{\frac{1}{2}}\left(\frac{l_{\text{coh}}}{1\,\text{Mpc}}\right)^{\frac{1}{2}}.$$

(10.39)

The angular deflection of extragalactic protons of $E \sim 10^{20}$ eV is small and one can hope to be able to do proton astronomy to find the sources or source regions of the highest-energy cosmic rays. Of course, due to the much larger magnetic fields in filaments and clusters of galaxies than in voids, particles are expected to undergo large magnetic deflection in the source region and only the propagation through voids will preserve the directional information.

The time delay follows from expanding the difference between length of a circular track segment and the total rectilinear distance traveled, $t_{\text{delay}} \approx d^3/(24c\, R_L^2)$. In the diffusion approach, the total time delay is given by

$$\langle t_{\text{delay}} \rangle \approx \frac{l_{\text{coh}}}{9c} \left(\frac{d}{R_L} \right)^2 \tag{10.40}$$

$$\approx 3.1 \times 10^5\, \text{yr} \left(\frac{Z\,B}{10^{-9}\,\text{G}} \right)^2 \left(\frac{10^{20}\,\text{eV}}{E} \right)^2 \left(\frac{d}{100\,\text{Mpc}} \right)^2 \left(\frac{l_{\text{coh}}}{1\,\text{Mpc}} \right).$$

There is no chance to have a coincident detection of gamma rays or neutrinos with charged cosmic rays for transient sources, i.e. sources that are active over timescales shorter than the typical time delay due to magnetic deflection.

At low energy, the time delays due to diffusion in extragalactic magnetic fields can be comparable to the age of the universe. This imposes a *magnetic horizon* on the source distance for lower-energy particles [335–337]. The maximum average distance d_{max} a particle can travel on a timescale of the age of the universe, $t_0 = 1/H_0$, can be written as

$$d_{\text{max}}^2 = \int_0^{t_0} D(E(t))\, \mathrm{d}t, \tag{10.41}$$

where D is the diffusion coefficient, which depends on the particle energy.

diffusion coefficient is given by the usual expression $D(E) = (1/3)\,c\,l_D$, where l_D is the diffusion length defined as length scale over which the angular deflection $\Delta\theta \sim 1$. With $\delta\theta \approx l_{\rm coh}/R_L$ we have a total deflection angle $\Delta\theta \sim \sqrt{N}\,\delta\theta$ after N steps of length $l_{\rm coh}$. The diffusion length is then given by the number of steps $N = l_D/l_{\rm coh}$ needed for $\Delta\theta \sim 1$ and we obtain

$$D(E) = \frac{1}{3}\,c\,l_D = \frac{1}{3}\,c\,\frac{R_L^2}{l_{\rm coh}} = \frac{1}{3}\,c\,l_{\rm coh}\left(\frac{E}{E_{\rm cr}}\right)^2, \qquad (10.42)$$

where we have introduced the critical energy at which the Larmor radius equals the coherence length $R_L(E_{\rm cr}) = l_{\rm coh}$. Numerically one has

$$E_{\rm cr} = 0.9 \times 10^{18}\,{\rm eV}\ Z\left(\frac{B}{\rm nG}\right)\left(\frac{l_{\rm coh}}{\rm Mpc}\right). \qquad (10.43)$$

For particles propagating over large timescales, the adiabatic expansion is the dominant energy loss process at low energy ($E \lesssim 10^{18}\,{\rm eV}$). Following Ref. [338] we use the approximation $(1/E)\,{\rm d}E/{\rm d}t = -H(z) \approx -H_0$. Inserting the time evolution of the particle energy

$$E(t) = E_{\rm src}\,e^{-H_0 t} \qquad (10.44)$$

in (10.41) and carrying out the integration we obtain

$$d_{\rm max}^2 \sim \frac{c\,l_{\rm coh}}{H_0}\left(\frac{E_{\rm src}}{E_{\rm cr}}\right)^2. \qquad (10.45)$$

in (10.41) and carrying out the integration we obtain

$$d_{\mathrm{max}}^2 \sim \frac{c\, l_{\mathrm{coh}}}{H_0} \left(\frac{E_{\mathrm{src}}}{E_{\mathrm{cr}}}\right)^2. \tag{10.45}$$

The magnetic horizon is less than $100\,\mathrm{Mpc}$ for protons with an injection energy $E_{\mathrm{src}} = 10^{18}\,\mathrm{eV}$ and a typical magnetic field strength of $1\,\mathrm{nG}$. As long as the distance covered by diffusion of particles over relevant timescales $\sim 1/H_0$ is larger than the distance between the sources, the locally observed flux is independent of the magnetic horizon (propagation theorem [339]). If the diffusion time of the closest sources at a distance $\sim d_s$ becomes comparable or exceeds the Hubble time, the contribution of extragalactic sources to the locally observed flux of cosmic rays will be suppressed. In first approximation, this effect is expected to be important at energies

$$E \lesssim Z \left(\frac{B}{\mathrm{nG}}\right) \left(\frac{l_{\mathrm{coh}}}{\mathrm{Mpc}}\right)^{\frac{1}{2}} \left(\frac{d_s}{70\,\mathrm{Mpc}}\right) 10^{18}\,\mathrm{eV} \tag{10.46}$$

for homogeneous magnetic field densities [337]. For a detailed estimate of the magnetic horizon effect one has to account for the inhomogeneous structure of extragalactic magnetic fields, in particular the presence of large voids [340].